Double reservoirs imaged below Great Sitkin Volcano, Alaska, explain the migration of volcanic seismicity

Xiaotao Yang[1], Diana C. Roman[2], Matthew M Haney[3], Cody Adam Kupres[1], Fan-Chi Lin[4], Ross Maguire[5], Helen Janiszewski[6], and Brandon Schmandt[7]

[1]Purdue University
[2]Carnegie Institution of Washington
[3]United States Geological Survey
[4]University of Utah
[5]University of Illinois at Urbana Champaign
[6]University of Hawaii at Manoa
[7]University of New Mexico

December 9, 2022

Abstract

Volcanic seismicity provides essential insights into the behavior of an active volcano across multiple time scales. However, to understand how magma moves as an eruption evolves, better knowledge of the geometry and physical properties of the magma plumbing system is required. In this study, using full-wave ambient noise tomography, we image the 3-D crustal shear-wave velocity structure below GreatSitkin Volcano in the central Aleutian Arc. The new velocity model reveals two low-velocity anomalies, which correlate with the migration of volcanic seismicity. With a partial melt of up to about 30%, these low-velocity anomalies are characterized as mushy magma reservoirs. We propose a six-stage eruption cycle to explain the migration of seismicity and the alternating eruption of two reservoirs with different recharging histories. The findings in this study have broad implications for the dynamics of magma plumbing systems and the structural control of eruption behaviors.

Double reservoirs imaged below Great Sitkin Volcano, Alaska, explain the migration of volcanic seismicity

Xiaotao Yang[1], Diana C. Roman[2], Matt Haney[3], Cody A. Kupres[1]

[1]Department of Earth, Atmospheric, and Planetary Sciences, Purdue University, West Lafayette, IN, USA.
[2]Earth and Planets Laboratory, Carnegie Institution for Science, Washington, DC, USA
[3]Alaska Volcano Observatory, USGS, Anchorage, AK, USA

Key Points:

- The pre- and co-eruptive seismicity below Great Sitkin Volcano, Alaska, shows a strong spatiotemporal migration
- A new 3-D shear-wave velocity model reveals two crustal low-velocity anomalies that correlate with the migrating seismicity
- We propose a six-stage eruption cycle involving two magma reservoirs to explain the long-term and short-term seismicity patterns

Corresponding author: Xiaotao Yang, `xtyang@purdue.edu`

Abstract

Volcanic seismicity provides essential insights into the behavior of an active volcano across multiple time scales. However, to understand how magma moves as an eruption evolves, better knowledge of the geometry and physical properties of the magma plumbing system is required. In this study, using full-wave ambient noise tomography, we image the 3-D crustal shear-wave velocity structure below Great Sitkin Volcano in the central Aleutian Arc. The new velocity model reveals two low-velocity anomalies, which correlate with the migration of volcanic seismicity. With a partial melt of up to about 30%, these low-velocity anomalies are characterized as mushy magma reservoirs. We propose a six-stage eruption cycle to explain the migration of seismicity and the alternating eruption of two reservoirs with different recharging histories. The findings in this study have broad implications for the dynamics of magma plumbing systems and the structural control of eruption behaviors.

Plain Language Summary

Understanding magma accumulation and transport systems below active volcanoes is essential for predicting eruption behavior and assessing the potential hazards. The distribution of earthquakes can partly be used to infer the development of magmatic activity at different times. However, to understand how magma moves at different stages of an eruption cycle, better knowledge of what the magma plumbing system looks like is necessary. In this study, we use an advanced seismic imaging method to construct the 3-D crustal shear-wave velocity structure below Great Sitkin Volcano in the central Aleutian Arc. The new velocity model reveals two crustal magma reservoirs, which correlate with the migration of seismicity. We propose a six-stage eruption cycle to explain the evolution of seismicity in space and time across the island and the alternating eruption of two reservoirs. The findings in this study help to understand better the control of eruption behaviors by the underlying magma plumbing system at active volcanoes.

1 Introduction

Magma plumbing systems of active volcanoes consist of magma storage reservoirs and conduits for transportation of magma to the surface (e.g., Tibaldi, 2015; Chaussard et al., 2013). The geometry and dynamics of magma plumbing systems play an essential role in controlling the eruption behavior. Magma plumbing systems possess a wide range of complexity in terms of the connection and interaction between multiple magma chambers (e.g., Tibaldi, 2015; Huang et al., 2015; Kiser et al., 2021), the lateral offset between reservoirs and the edifice (e.g., Tibaldi, 2015; Lerner et al., 2020), the geochemical evolution of the magma (e.g., Spera, 2004), and the development of eruptive activity in an eruption cycle (e.g., Tibaldi, 2015; Chaussard et al., 2013; Roman & Cashman, 2018; Paulatto et al., 2022). Among these complexities, it is important to understand how magma moves in space and time during an eruption and between eruptions and what controls this process. We address these questions by investigating Great Sitkin Volcano in central Aleutian Arc in Alaska (Figure 1a) (e.g., Miller et al., 1998; Waythomas et al., 2003), which erupted on 26 May 2021 with ongoing effusive lava flows as of the time of writing (Global Volcanism Program, 2022a). Great Sitkin Volcano is an oval-shaped stratovolcano with a collapsed caldera (Waythomas et al., 2003) and an edifice aperture of about 8 by 11 km (Figure 1a) (Miller et al., 1998). The volcanic rocks are dominantly andesites to basaltic andesites (Miller et al., 1998; Waythomas et al., 2003). The ongoing eruption started as an explosive eruption on 26 May 2021 and was preceded by multiple phreatic explosions between June 2018 and February 2019. The 26 May 2021 eruption was followed by a dome emplacement that peaked in growth rate during August through September (Global Volcanism Program, 2022b, 2022a; Marchese & Genzano, 2022).

Seismic activity at volcanoes helps to reveal the evolution of the eruption activity (e.g., Power et al., 2004; Roman et al., 2004; Scandone et al., 2007; Pesicek et al., 2008; Roman & Cashman, 2018). At Great Sitkin, volcanic earthquakes (5/1/2020-9/5/2022) are primarily concentrated along an NW-SE trending zone (Figure 1a). This seismic zone delineates an inverse-V shape in depth, with the shallowest earthquakes below the caldera summit and the 2021 eruption vent (Figure 1a and b). Locations of the pre- and co-eruptive seismicity suggest the migration of magmatic activity (Figure 1b-d). Approximately 24 hours before the 26 May 2021 eruption, seismicity started to increase abruptly (Figure 1c) with a swarm of earthquakes northwest of the edifice (swarm-1 in Figure 1a-b). About two months later, a second earthquake swarm (swarm-2) occurred further to the southeast. Interestingly, about one year after the initial eruption, there was another earthquake swarm (swarm-3) northwest of the edifice, generally at greater depth than swarm-1 earthquakes. In the longer term (Figure 1d), there was an earthquake cluster in early 2002 through 2004 southeast of the edifice (Pesicek et al., 2008). Pesicek et al. (2008) and Power et al. (2004) argue that this cluster of volcano-tectonic earthquakes and the co-occurring long-period events are evidence of a magma intrusion. This elevated seismicity (Figure 1d) suggests that the reservoir to the southeast of the volcano edifice may have begun recharging as early as 2002, reaching its peak in 2020. In contrast, to the northwest of the volcano edifice, there was a slight increase in seismicity in 2018, followed by a relatively seismically quiet period in 2020 until the day before the eruption (Global Volcanism Program, 2022b). However, it is not clear how the migration of seismicity is linked to the geometry and dynamics of the magma plumbing system.

We investigate structural controls of the spatial-temporal migration of seismicity at Great Sitkin Volcano and the associated eruption stages. We construct a 3-D shear-wave velocity model for the upper 6 km of the crust below sea level (BSL) under Great Sitkin, using a full-wave ambient noise tomography method. The new shear-wave velocity model reveals two low-velocity anomalies at 1.5-4.5 km BSL and 3-6 km BSL to the southeast and northwest of the volcano edifice, respectively. These low-velocity anomalies correspond to up to approximately 30% partial melts and are thus characterized as mushy magma

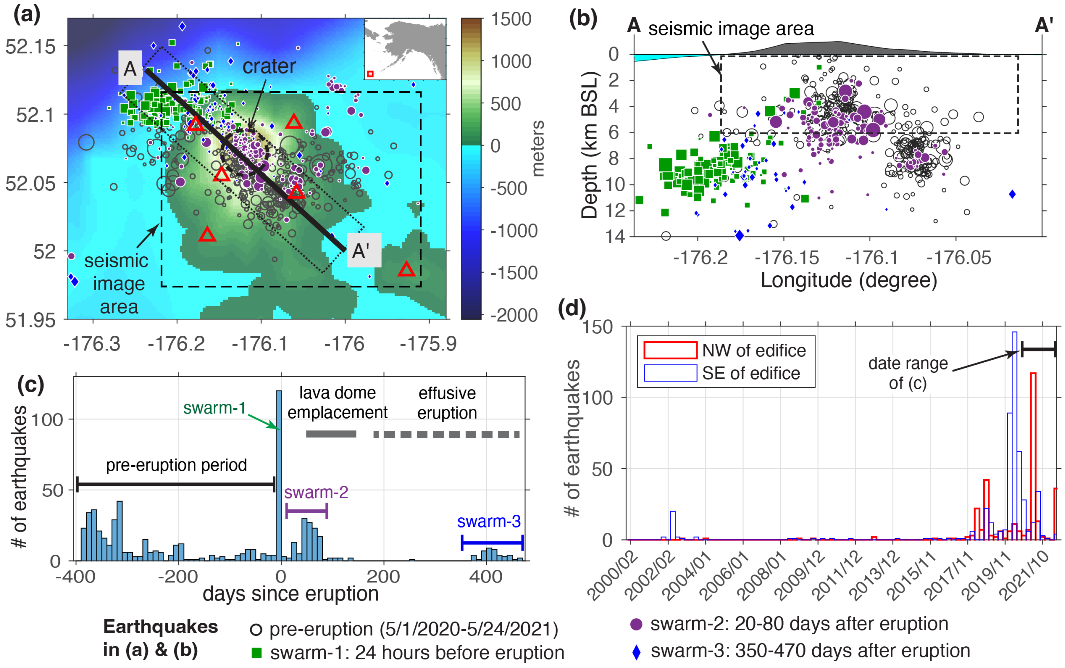

Figure 1. Distribution of earthquakes around Great Sitkin Volcano between different time periods. (a) Earthquake epicenters (magnitude ≥ 0) from the USGS Comprehensive Earthquake Catalog (ComCat) (U.S. Geological Survey, 2022) from May 2020 to September 2022, scaled by magnitude. The main explosive eruption occurred at 5:04 UTC on 26 May 2021. The pre-eruption earthquakes (5/1/2020-5/24/2021) are shown as open circles. Swarm-1 (green squares) refers to earthquakes within approximately 24 hours before the 26 May 2021 eruption. Swarm-2 (purple dots) includes earthquakes 10-100 days after the initial eruption. Swarm-3 (blue diamonds) contains earthquakes 300-470 days after the initial eruption. Triangles are seismic stations from the Alaska Volcano Observatory network (network code: AV) used in this study (Alaska Volcano Observatory/USGS, 1988). The dashed box shows the seismic imaging area. (b) Depth distribution of the earthquakes along profile A-A' highlighting the three earthquake swarms. The dashed box shows the seismic imaging area. BSL: below sea level. (c) Histogram with 10-day bins showing the variation of seismicity within 2 km from profile A-A', shown as the dotted box in (a). The three earthquake swarms are labeled along with the key development phases of the eruption. (d) Histograms with 90-day bins showing the longer-term variations of seismicity between 1/1/2000 and 9/5/2022 to the northwest (thick red bars) and southeast (thin blue bars) of the volcano edifice. The earthquakes below the crater atop the edifice, with the lateral extent defined by the dashed circle in (a), are excluded in (d).

reservoirs. We propose a six-stage eruption cycle to explain the spatiotemporal migration of the volcanic seismicity at Great Sitkin.

2 Data and Methods

2.1 Empirical Green's functions

Empirical Green's functions between two seismic stations can be retrieved from the cross-correlations of ambient noise waveforms. We use the *SeisGo* Python toolbox to download the continuous seismic waveforms and compute the cross-correlations (Yang et al., 2022). The Alaska Volcano Observatory operates six broadband seismic stations on Great Sitkin Island and nearby Igitkin Island (network code: AV; triangles in Figure 1a) (Alaska Volcano Observatory/USGS, 1988). We download the vertical continuous waveforms from these stations between 7/1/2019 and 8/1/2020 from the IRIS Data Management Center. We downsample the waveforms at the rate of 20 Hz, followed by the removal of the instrument responses.

We slice the continuous waveforms into 4-hour segments with a step of 2 hours and normalize the amplitude spectrum of each segment using the moving average method, as described by Bensen et al. (2007). We attempt to further eliminate transient signals by discarding segments with peak amplitudes greater than 10 times the standard deviation of all segments within each downloaded 3-day block, following Jiang and Denolle (2020). We then compute the cross-correlations in the frequency domain following Viens et al. (2017). We calculate the stacks of the cross-correlations across the entire duration and within each 30-day window to provide uncertainties of the phase delay measurements in Section 2.2. The empirical Green's functions are computed as the negative time derivative of the cross-correlations.

2.2 Full-wave ambient noise tomography

We apply the full-wave ambient noise tomography method, which involves full-wavefield simulation, to invert for the velocity perturbations using finite-frequency kernels (e.g., Gao & Shen, 2012, 2014; Yang & Gao, 2018, 2020). The tomography method accounts for the cross-dependence of Rayleigh waves to both P and S wave velocities (Z. Zhang & Shen, 2008). We first simulate the wave propagation in the 3-D spherical Earth using a nonstaggered-grid, finite-difference method (W. Zhang et al., 2012), with a grid spacing of 0.001 and 0.0013 degrees in the latitudinal and longitudinal directions, respectively. The vertical grid spacing increases with depth from 0.037 km at the surface to 0.022 km at the depth of 28 km. We use the global velocity model by Shapiro and Ritzwoller (2002) as the reference model. We then measure the Rayleigh wave phase delays between the synthetics and the observed empirical Green's functions through cross-correlations in eight overlapping period ranges, including 0.6-1s, 0.8-1.25s, 1-1.5s, 1.25-1.8s, 1.5-2s, 1.8-2.5s, 2-3s, and 2.5-3.5s. Before measuring the phase delays, we discard empirical Green's functions with signal-to-noise ratios below 3. The phase delay measurements with correlation coefficients $\geq$ 0.6 are used in the kernel calculation and inversion. The reference velocity model is progressively updated for four iterations until major velocity features converge to achieve the final model.

3 Results: Shear-Wave Velocity Model

The shear-wave velocity model reveals two low-velocity features at different depths aligning in the northwest-southeast direction (L1 and L2 in Figure 2). At a depth of 2 km (Figure 2a-b), we observe a prominent, localized low-velocity feature (1-1.2 km/s) beneath station GSMY (anomaly L1). This anomaly extends down to about 3-4 km BSL, where the velocity is about 1.5-2.1 km/s (Figure S1a). At greater depths (Figures 2c and S1a), the velocity generally decreases toward the northwest with a low-velocity anomaly of 2.2-2.6 km/s in the broad region below station GSSP (anomaly L2). The vertical velocity cross-section A-A' (NW-SE across the island) shows the separation of these two low-velocity anomalies (with up to -10% perturbations) in both lateral and vertical directions (Figure 2d). Both of these two low-velocity anomalies, particularly L1, appear to be dipping to the northwest (Figure 2d), though the top of the L1 anomaly is not well-constrained. The NW-SE alignment of these two low-velocity anomalies is consistent with the location of the NW-SE trending seismic zone (Figures 1a and 2a-c). The cross-sections along profiles B-B' and C-C' show that the L1 low-velocity anomaly is localized in the SW-NE direction and is bounded by higher velocities extending down to at least 6 km BSL, below which our resolution is dramatically decreased, as described below.

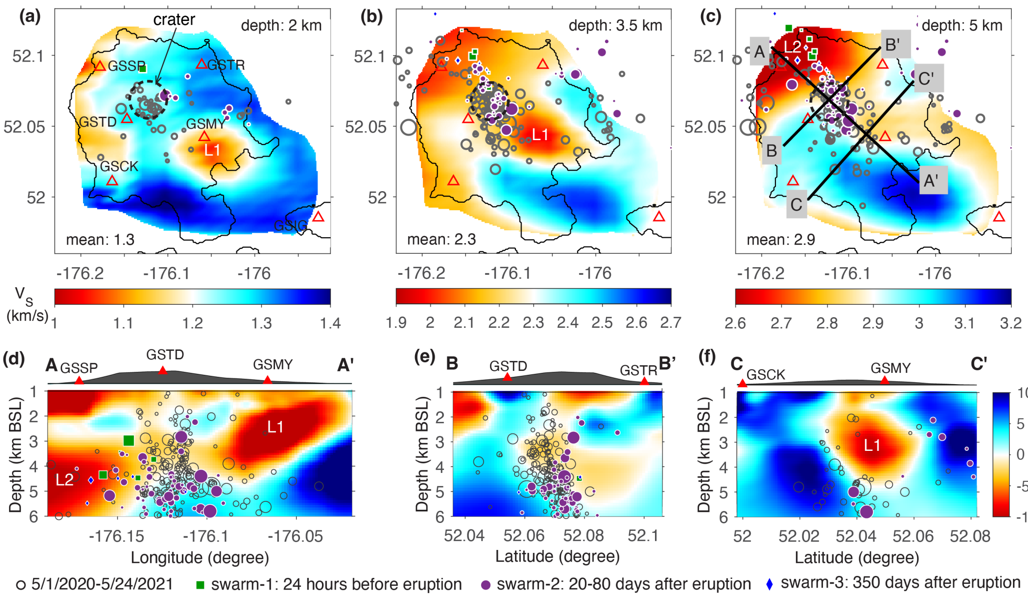

Figure 2. Shear-wave velocity model of Great Sitkin. (a)-(c) Velocity depth slices at 2 km, 3.5 km, and 5 km BSL, respectively. The average velocity at each depth is given in the lower-left corner of each panel. The triangles are AV seismic stations. Earthquakes are projected about ±1 km around the slice depth, scaled by magnitudes. Gray circles are earthquakes between 5/1/2020 and 5/24/2021. Earthquake swarm-1 (green squares), swarm-2 (purple dots), and swarm-3 (blue diamonds) are shown for reference, color-coded the same as Figure 1a. The dashed circle marks the extent of the crater atop the volcano edifice. L1 and L2 label the two key low-velocity features. (d)-(f) Vertical cross-sections of the shear-wave velocity model at 1-6 km BSL, showing the velocity perturbations relative to the average velocity at each depth. Since the absolute velocities span across a wide range from 1 km/s to about 3.5 km/s (Figure S1), we use perturbations to highlight the velocity anomalies. Earthquakes are projected within about 2 km away from each profile, color-coded as in (a)-(c). See panel (c) for the profile locations.

The checkerboard resolution tests (Figure S3) and model recovery tests (Figure S4) suggest that our best resolution is for the depth range of 2-5 km BSL, degrading dramatically at greater depths. We can resolve the geometry of velocity anomalies with a horizontal scale of >3.5 km and a vertical scale of > 2 km. In addition, L1 can be resolved much better than L2 (Figure S4). In later sections, when analyzing the absolute velocities or perturbation amplitudes, we focus more on the L1 anomaly. See Text S1 in the supplement for a detailed resolution analysis.

4 Discussion

4.1 Correlation with seismicity

The key features in the new velocity model show a strong correlation with the earthquake activity below Great Sitkin Island. The earthquakes from 5/1/2020 to 9/5/2022 are concentrated between these two low-velocity anomalies mainly at the depth of > 2 km BSL (L1 and L2 in Figure 2d). The centers of both L1 and L2 anomalies are relatively aseismic (Figure 2d and f). Below the depth of 4 km, the earthquakes are concentrated along relatively large velocity gradients (Figure 2d). This concentration pattern has been observed at other active volcanoes, such as Mount St. Helens Volcano in the Cascadia volcanic arc (e.g., Barker & Malone, 1991; Kiser et al., 2016), Mount Spurr Volcano in southwestern Alaska (Power et al., 1998), the Hawaiian volcanoes (Lin et al., 2014), Redoubt Volcano in Alaska (Benz et al., 1996), Stromboli Volcano in Italy (Patanè et al., 2017), Mount Rainier Volcano in Cascadia (Flinders & Shen, 2017), and the Gakkel Ridge volcanic complex (Korger & Schlindwein, 2014). The occurrence of earthquakes along velocity gradients below volcanic areas is commonly attributed to the stress concentration at structural boundaries resulting from magma movement or dike intrusion (e.g., Korger & Schlindwein, 2014; Barker & Malone, 1991; Roman et al., 2004; Kiser et al., 2016).

The earthquake swarms before and after the 26 May 2021 initial eruption provides insights into the eruption dynamics. Occurring right before the eruption, swarm-1 earthquakes may delineate the magma pathway (with a relatively fast ascent rate)for the initial eruption, suggesting it was sourced from the L2 reservoir. Swarm-2 earthquakes occurred during the dome emplacement period (late July 2021 through November 2021; Figure 1c), primarily along the velocity gradient at the bottom of the L1 anomaly and below the edifice. This spatiotemporal coincidence indicates that the L1 anomaly may be linked to the dome emplacement. The seismicity at a shallower depth (i.e., < 2 km BSL) likely delineates shallow magma conduits, which seem to be shared by swarm-1 and swarm-2 (Figure 1b). However, the detailed geometry and velocity of the shallow conduit are not resolvable in our model. The distinct difference in the inferred intrusion timelines between the southeast and the northwest of the edifice is coincident with the spatial separation of the two low-velocity anomalies (L1 and L2) below these two regions.

4.2 Double magma reservoirs

There are multiple mechanisms that can reduce shear-wave velocities at active volcanoes, including high-temperature anomalies (e.g., Kern et al., 2001), volatiles (water and gas) (e.g., Ito, 1990; Chu et al., 2010; Christensen & Stanley, 2003), and partial melts (e.g., Avellaneda, 1987; Berryman, 1998; Norris, 1985; Takei, 2002; Paulatto et al., 2022). Considering the surface heat flow and the distribution of geothermal features at Great Stikin Island, the contributions from temperature anomalies to the L1 and L2 low-velocity anomalies should be minor (see Text S2 in the supplement). Water and gas are likely to play an important role in reducing the shear-wave velocities, though the exact contribution is not well constrained with the current data on water content and gas emissions (e.g., Fischer et al., 2021). On the other hand, partial melts are commonly used to explain seismic low velocities below active volcanoes (e.g., Lees, 2007; Lin et al., 2014; Power et al., 1998; Jaxybulatov et al., 2014; Kiser et al., 2016; Ward et al., 2017; Delph et al., 2017; Paulatto et al., 2022). With the ongoing eruption of the Great Sitkin Volcano, it is reasonable to assume partial melts as the dominant factor responsible for the velocity reduction of the L1 and L2 anomalies.

The melt fraction estimates for L1 and L2 low-velocity anomalies suggest that they are mushy magma reservoirs with up to approximately 30% partial melts. At Great Sitkin, the volcanic deposits are dominantly andesite and basaltic andesite (Miller et al., 1998; Loewen, 2021). We compute the melt fractions following the workflow and computer codes by Paulatto et al. (2022) using the Self-Consistent Scheme (Figure S5a) (e.g, Berryman, 1998; Paulatto et al., 2022) and the Differential Effective Medium (Figure S5b) (e.g., Norris, 1985; Avellaneda, 1987; Paulatto et al., 2022) methods. We use velocities for crystal and molten andesite based on the experimental data by Christensen and Stanley (2003), Ueki and Iwamori (2016), and Takei (2002) (see Text S3 in the supplement for key parameters). The estimated melt fractions are about 0.23 ± 0.1 and about 0.11 ± 0.05 for the L1 and L2 anomalies, respectively. Because of the limited resolution in recovering the synthetic L2 anomaly (Text S1), the uncertainty of the melt fraction for L2 is relatively large. It is worth noting that these estimates are the upper limits without considering volatiles. Measurements of the volatile contents from this volcano, as done for other volcanoes along the Aleutian

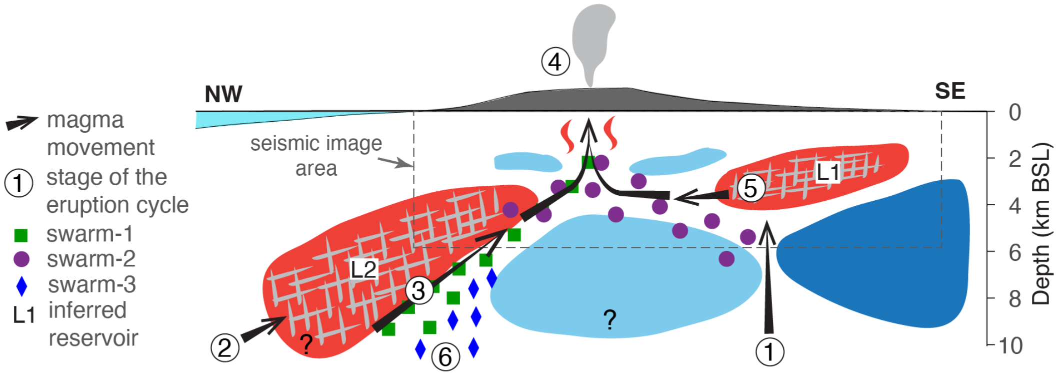

Figure 3. Schematic model showing the six-stage evolution of the 2021-present eruption of the Great Sitkin Volcano. Stage-1: recharge of the L1 reservoir southeast of the edifice. Stage-2: recharge of the L2 reservoir northwest of the edifice. Stage-3: magma ascent and intense fracturing along the lower boundary of the L2 reservoir. Stage-4: explosive eruption with magma primarily from the L2 reservoir. Stage-5: initial dome emplacement with magma primarily from the L1 reservoir. Stage-6: prolonged effusive eruption with magma sourced from the L2 reservoir. The structures within the dashed box are interpreted based on cross-section A-A' (Figure 2d). The question marks denote extrapolated structures that are not constrained by the velocity model.

Arc (Fischer et al., 2019, 2021), would help refine the melt estimates. Nevertheless, the partial melts within the L1 and L2 anomalies are evidence of mushy magma reservoirs.

4.3 A six-stage eruption cycle

The spatial and temporal migration of seismicity before and after the 26 May 2021 explosive eruption (Figure 1) indicates a complicated eruption cycle, spanning at least 20 years. This eruption cycle likely consists of multiple stages, with added complexity from the interaction of the two inferred magma reservoirs. Previous studies have proposed several models to explain multi-stage magma unrest and eruption based on seismicity (e.g., Roman & Cashman, 2018), surface deformation (e.g., Chaussard et al., 2013), and petrological and geochemical characteristics (e.g., Spera, 2004; Sparks et al., 2019). However, these models mostly focus on the vertical migration of magma activity as the eruption cycle evolves. They cannot explain the bi-modal behaviors of the spatially separated (both laterally and vertically) magma reservoirs below Great Sitkin Volcano.

We propose a six-stage eruption cycle for the 26 May 2021 eruption of the Great Sitkin Volcano, involving the imaged deep (L2) and shallow (L1) reservoirs (Figure 3). This model explains the observations from both long- and short-term seismicity (Figure 1) and seismic velocity structures (Figure 2). It is a refined development of the seismicity and geochemical evolution models by Spera (2004) and Roman and Cashman (2018). The key development of our model is the consideration of the interaction and alternation between magma reservoirs. We describe the six stages of the eruption cycle in the following paragraphs.

Stage-1: Recharge of the shallow reservoir (L1). At this stage, the shallow (L1) reservoir southeast of the edifice associated with L1 low-velocity anomaly starts to recharge, as inferred from the cluster of earthquakes and long-period events (Power et al., 2004; Pesicek et al., 2008). The magma is likely fed through a nearly vertical pathway down to at least 12 km, which is the bottom of the earthquake cluster (Pesicek et al., 2008). Although the resolution is low, this pathway might align with the northwestern boundary of the relatively high velocities below the L1 reservoir (Figure 2d). The recharge of the

L1 reservoir reaches its peak intensity in 2020, corresponding to the elevated seismicity in late 2020 that decreased in early 2021 (Figure 1d). It is worth noting that Pesicek et al. (2008) also identified another cluster of earthquakes in March 2002 about 20 km to the west of the volcano edifice at the depth of >10 km BSL (beyond our study area). Although they argue that these earthquakes are not volcanic events, we cannot completely rule out the possibility of magma intrusion at this location based on current constraints. Therefore, there is a slight chance that there was another magma intrusion in early 2002 further to the west of the edifice (west of the L2 reservoir).

Stage-2: Recharge of the deep reservoir (L2). About 15-16 years after the initial recharge of the L1 reservoir, the L2 reservoir west-northwest of the volcano edifice starts to recharge in late 2017. The recharging process is accompanied by a moderate increase in earthquake activity lasting through 2020 (Figure 1d). In contrast to the recharge of the L1 reservoir, the lapse is much shorter for the L2 reservoir between the initial recharge and the eruption. Stages 1 and 2 correspond to the staging phase by Roman and Cashman (2018) and Spera (2004) but happen at two reservoirs. The current data is insufficient to evaluate the potential connection of the deep sources feeding these two reservoirs.

Stage-3: Rapid magma ascent from the L2 reservoir. As magma recharge continues, the pressure within the L2 reservoir slowly builds up to the critical value, causing intensive fracturing and accelerated ascent of the magma along the lower boundary of the L2 reservoir. This boundary, with fractures, serves as the pathway for magma to quickly move toward the volcano summit. This magma pathway is delineated by NW-dipping swarm-1 seismic zone and a relatively large seismic velocity gradient (Figure 2d).

Stage-4: Explosive eruption sourced from the L2 reservoir. The intense fracturing and magma ascent processes lead to an explosive eruption within 24 hours. Based on the location of swarm-1 earthquakes, the eruption at this stage is driven mostly by the magma activity of the L2 reservoir. The drop in seismicity in this region in late 2020, likely associated with the L1 reservoir, suggests a possible depressurization, such as through inflation (e.g., Chaussard et al., 2013). However, more data on surface deformation is needed to test this hypothesis.

Stage-5: Dome formation sourced from the L1 reservoir. About 2 months following the initial eruption, an intensive dome emplacement phase begins, accompanied by a swarm of earthquakes generally below the L1 and L2 reservoirs (swarm-2) (Figure 1c). As implied by the seismicity, the dome emplacement might be driven by the magma from both reservoirs, explaining the rapid dome growth from July to October 2021 (Global Volcanism Program, 2022a). However, most of the swarm-2 earthquakes are located below the L1 reservoir, suggesting that the L1 reservoir dominates the magma activity at this stage. This stage is an important development compared to previously proposed eruption cycles (e.g., Roman & Cashman, 2018; Spera, 2004; Chaussard et al., 2013), as it implies dynamic interaction between the reservoirs. Specifically, the eruption and fast magma transport of the L2 reservoir may have created fractures that helped to unseal the L1 reservoir. The magma moves toward the conduits even when the pressure is below the critical point with relatively low seismicity. This explains why the dome emplacement is more effusive than explosive. Eruption modeling and petrological analyses (e.g. Larsen et al., 2013; Biggs et al., 2016), which are outside the scope of this study, would help examine this phenomenon of successive tapping of two reservoirs during the eruption. The conduits or fractures produced by the explosive eruption of the L2 reservoir would make it easy for the magma in the L1 reservoir to flow out. Nevertheless, the lateral transport of magma is commonly seen or proposed at other volcanoes (e.g., Tibaldi, 2015; Lerner et al., 2020; Kiser et al., 2021). A more detailed seismic imaging with improved station coverage is required to narrow down the explanations.

Stage-6: Resurgence of the deeper L2 reservoir. As the eruption becomes more effusive and dome emplacement slows down, magmatic activity switches back to the deeper

L2 reservoir. This is supported by a cluster of small earthquakes below the L2 reservoir (swarm-3), overall deeper than swarm-1 earthquakes. The magma activity in the L1 reservoir decays during this stage. Stages 3-6 involve a model of two active reservoirs that alternate as sources of the eruption.

4.4 Future studies

With two magma reservoirs, migrating volcanic seismicity, and a collapsed caldera, Great Sitkin Volcano provides an ideal natural laboratory to study the dynamics of magma plumbing systems and volcanic hazards. Due to the limited data coverage, there are several remaining questions to be addressed by future studies about the eruption dynamics at Great Sitkin with multi-disciplinary observations. A better constraint on the lateral and depth scales of the L2 reservoir requires a larger aperture seismic array. Denser station coverage is needed to image the distribution of shallow magma conduits below the summit and to understand their control of magma transport and the eruption explosivity. Data on surface deformation (e.g., InSAR mapping) would help to examine the surface inflation and deflation corresponding to different eruption stages. The record of surface temperature over the past several years and its spatial distribution would help refine the temperature anomaly at different stages as well as the estimate of melt fractions. Measurements of volatile emissions from the volcano would also improve melt fraction estimates. In addition, a high-resolution gravity survey is required to delineate the heterogeneity of density below the island.

5 Conclusions

The geometry and dynamics of magma plumbing systems play an essential role in controlling the eruption behavior of active volcanoes. Furthermore, the distribution of earthquakes provides essential insights into the magma transport below the volcano. At Great Sitkin Volcano in the central Aleutian Arc, Alaska, which erupted on 26 May 2021 and continues with ongoing effusive lava flows, the seismicity patterns during the past two decades show a strong migration across the volcanic island from northwest to southeast of the edifice. Multiple swarms of earthquakes have occurred at different locations as the eruption cycle evolved. We construct a 3-D crustal shear-wave velocity model of Great Sitkin Island for the upper 6 km of the crust BSL, which reveals two low-velocity anomalies corresponding to mushy magma reservoirs with up to approximately 30% partial melts. We propose a six-stage eruption cycle to explain the migration of seismicity and the alternating eruption of the two reservoirs with different recharging histories. The findings in this study have broad implications for the dynamics of magma plumbing systems and the structural control of eruption behavior.

Open Research

The seismic waveforms from the Alaska Volcano Observatory network (Alaska Volcano Observatory/USGS, 1988) were downloaded from IRIS Data Management Center (`https://ds.iris.edu/ds/nodes/dmc/`) and processed using *SeisGo* (`https://doi.org/10.5281/zenodo.5873724`), built upon *ObsPy* (Beyreuther et al., 2010) and *NoisePy* (Jiang & Denolle, 2020).

Acknowledgments

This research has been funded by the startup funding of Purdue University for Xiaotao Yang. ***Author Contributions:*** X. Yang contributed to conceptualization, supervision, funding acquisition, data curation, methodology, formal analysis, interpretation, and writing of the original draft. D. Roman, M. Haney, and C. Kupres all contributed to the interpretation and reviewing and editing of the manuscript.

References

Alaska Volcano Observatory/USGS. (1988). *Alaska Volcano Observatory* (Tech. Rep.). Anchorage, AK: International Federation of Digital Seismograph Networks. doi: 10.7914/SN/AV

Avellaneda, M. (1987, 9). Iterated homogenization, differential effective medium theory and applications. *Communications on Pure and Applied Mathematics*, *40*, 527-554. Retrieved from `https://onlinelibrary.wiley.com/doi/full/10.1002/cpa.3160400502` doi: 10.1002/CPA.3160400502

Barker, S. E., & Malone, S. D. (1991, 7). Magmatic system geometry at Mount St. Helens modeled from the stress field associated with posteruptive earthquakes. *Journal of Geophysical Research*, *96*, 11883. Retrieved from `http://doi.wiley.com/10.1029/91JB00430` doi: 10.1029/91JB00430

Bensen, G. D., Ritzwoller, M. H., Barmin, M. P., Levshin, A. L., Lin, F., Moschetti, M. P., ... Yang, Y. (2007). Processing seismic ambient noise data to obtain reliable broadband surface wave dispersion measurements. *Geophysical Journal International*, *169*, 1239-1260. doi: 10.1111/j.1365-246X.2007.03374.x

Benz, H. M., Chouet, B. A., Dawson, P. B., Lahr, J. C., Page, R. A., & Hole, J. A. (1996, 4). Three-dimensional *P* and *S* wave velocity structure of Redoubt Volcano, Alaska. *Journal of Geophysical Research: Solid Earth*, *101*, 8111-8128. Retrieved from `http://doi.wiley.com/10.1029/95JB03046` doi: 10.1029/95JB03046

Berryman, J. G. (1998, 6). Long-wavelength propagation in composite elastic media ii. ellipsoidal inclusions. *The Journal of the Acoustical Society of America*, *68*, 1820. Retrieved from `https://asa.scitation.org/doi/abs/10.1121/1.385172` doi: 10.1121/1.385172

Beyreuther, M., Barsch, R., Krischer, L., Megies, T., Behr, Y., & Wassermann, J. (2010, 05). ObsPy: A Python Toolbox for Seismology. *Seismological Research Letters*, *81*(3), 530-533. Retrieved from `https://doi.org/10.1785/gssrl.81.3.530` doi: 10.1785/gssrl.81.3.530

Biggs, J., Robertson, E., & Cashman, K. (2016, 4). The lateral extent of volcanic interactions during unrest and eruption. *Nature Geoscience*, *9*, 308-311. Retrieved from `http://www.nature.com/articles/ngeo2658` doi: 10.1038/ngeo2658

Chaussard, E., Amelung, F., & Aoki, Y. (2013, 8). Characterization of open and closed volcanic systems in Indonesia and Mexico using InSAR time series. *Journal of Geophysical Research: Solid Earth*, *118*, 3957-3969. Retrieved from `https://onlinelibrary.wiley.com/doi/full/10.1002/jgrb.50288https://onlinelibrary.wiley.com/doi/abs/10.1002/jgrb.50288https://agupubs.onlinelibrary.wiley.com/doi/10.1002/jgrb.50288` doi: 10.1002/JGRB.50288

Christensen, N. I., & Stanley, D. (2003). Seismic velocities and densities of rocks. *International Geophysics*, *81*, 1587-1594. doi: 10.1016/S0074-6142(03)80278-4

Chu, R., Helmberger, D. V., Sun, D., Jackson, J. M., & Zhu, L. (2010, 1). Mushy magma beneath yellowstone. *Geophysical Research Letters*, *37*. doi: 10.1029/2009GL041656

Delph, J. R., Ward, K. M., Zandt, G., Ducea, M. N., & Beck, S. L. (2017). Imaging a magma plumbing system from mash zone to magma reservoir. *Earth and Planetary Science Letters*, *457*, 313-324. Retrieved from `www.elsevier.com/locate/epsl` doi: 10.1016/j.epsl.2016.10.008

Fischer, T. P., Arellano, S., Carn, S., Aiuppa, A., Galle, B., Allard, P., ... Chiodini, G. (2019, 12). The emissions of CO_2 and other volatiles from the world's subaerial volcanoes. *Scientific Reports 2019 9:1*, *9*, 1-11. Retrieved from `https://www.nature.com/articles/s41598-019-54682-1` doi: 10.1038/s41598-019-54682-1

Fischer, T. P., Lopez, T. M., Aiuppa, A., Rizzo, A. L., Ilanko, T., Kelley, K. A., & Cottrell, E. (2021, 12). Gas emissions from the western Aleutians volcanic arc. *Frontiers in Earth Science*, *9*, 1205. Retrieved from `https://www.frontiersin.org/articles/10.3389/feart.2021.786021/full` doi: 10.3389/feart.2021.786021

Flinders, A. F., & Shen, Y. (2017, 12). Seismic evidence for a possible deep crustal hot zone beneath southwest Washington. *Scientific Reports*, *7*, 7400. Retrieved from http://www.nature.com/articles/s41598-017-07123-w doi: 10.1038/s41598-017-07123-w

Gao, H., & Shen, Y. (2012). Validation of shear-wave velocity models of the Pacific Northwest. *Bulletin of the Seismological Society of America*, *102*, 2611-2621. doi: 10.1785/0120110336

Gao, H., & Shen, Y. (2014). Upper mantle structure of the Cascades from full-wave ambient noise tomography: Evidence for 3d mantle upwelling in the back-arc. *Earth and Planetary Science Letters*, *390*, 222-233. doi: 10.1016/j.epsl.2014.01.012

Global Volcanism Program. (2022a, May). *Report on Great Sitkin (United States)* (Vol. 47) (No. 5). Smithsonian Institution.

Global Volcanism Program. (2022b, September). *Report on Great Sitkin (United States)* (Vol. 43) (No. 9). Smithsonian Institution. Retrieved from https://doi.org/10.5479/si.GVP.BGVN201809-311120

Huang, H. H., Lin, F. C., Schmandt, B., Farrell, J., Smith, R. B., & Tsai, V. C. (2015). The Yellowstone magmatic system from the mantle plume to the upper crust. *Science*, *348*, 773-776. doi: 10.1126/science.aaa5648

Ito, K. (1990, 1). Effects of H_2O on elastic wave velocities in ultrabasic rocks at 900°C under 1 GPa. *Physics of the Earth and Planetary Interiors*, *61*, 260-268. Retrieved from https://linkinghub.elsevier.com/retrieve/pii/003192019090110J doi: 10.1016/0031-9201(90)90110-J

Jaxybulatov, K., Shapiro, N. M., Koulakov, I., Mordret, A., Landes, M., & Sens-Schonfelder, C. (2014, 10). A large magmatic sill complex beneath the Toba caldera. *Science*, *346*, 617-619. Retrieved from https://www.sciencemag.org/lookup/doi/10.1126/science.1258582 doi: 10.1126/science.1258582

Jiang, C., & Denolle, M. A. (2020). Noisepy: A new high-performance python tool for ambient-noise seismology. *Seismological Research Letters*. Retrieved from https://pubs.geoscienceworld.org/ssa/srl/article/583390/NoisePy-A-New-HighPerformance-Python-Tool-for doi: 10.1785/0220190364

Kern, H., Popp, T., Gorbatsevich, F., Zharikov, A., Lobanov, K., & Smirnov, Y. (2001, 8). Pressure and temperature dependence of v_p and v_s in rocks from the superdeep well and from surface analogues at kola and the nature of velocity anisotropy. *Tectonophysics*, *338*, 113-134. Retrieved from https://linkinghub.elsevier.com/retrieve/pii/S0040195101001287 doi: 10.1016/S0040-1951(01)00128-7

Kiser, E., Levander, A., Schmandt, B., & Hansen, S. (2021, 3). Seismic evidence of bottom-up crustal control on volcanism and magma storage near Mount St. Helens. *Geophysical Research Letters*, *48*, e2020GL090612. Retrieved from https://onlinelibrary.wiley.com/doi/full/10.1029/2020GL090612https://onlinelibrary.wiley.com/doi/abs/10.1029/2020GL090612https://agupubs.onlinelibrary.wiley.com/doi/10.1029/2020GL090612 doi: 10.1029/2020GL090612

Kiser, E., Palomeras, I., Levander, A., Zelt, C., Harder, S., Schmandt, B., ... Ulberg, C. (2016). Magma reservoirs from the upper crust to the moho inferred from high-resolution v_p and v_s models beneath Mount St. Helens, Washington State, USA. *GEOLOGY*, *44*. Retrieved from www.geosociety.org/pubs/ft2016.htm, doi: 10.1130/G37591.1

Korger, E., & Schlindwein, V. (2014, 1). Seismicity and structure of the 85°E volcanic complex at the ultraslow spreading Gakkel Ridge from local earthquake tomography. *Geophysical Journal International*, *196*, 539-551. Retrieved from http://academic.oup.com/gji/article/196/1/539/592594/Seismicity-and-structure-of-the-85E-volcanic doi: 10.1093/gji/ggt390

Larsen, J. F., Śliwiński, M. G., Nye, C., Cameron, C., & Schaefer, J. R. (2013, 8). The 2008 eruption of Okmok Volcano, Alaska: Petrological and geochemical constraints on the subsurface magma plumbing system. *Journal of Volcanology and Geothermal Research*, *264*, 85-106. Retrieved from https://linkinghub.elsevier.com/retrieve/pii/S0377027313002217 doi: 10.1016/j.jvolgeores.2013.07.003

Lees, J. M. (2007, 11). Seismic tomography of magmatic systems. *Journal of Volcanology and Geothermal Research*, *167*, 37-56. Retrieved from https://linkinghub.elsevier.com/retrieve/pii/S0377027307001965 doi: 10.1016/j.jvolgeores.2007.06.008

Lerner, A. H., O'Hara, D., Karlstrom, L., Ebmeier, S. K., Anderson, K. R., & Hurwitz, S. (2020, 7). The prevalence and significance of offset magma reservoirs at arc volcanoes. *Geophysical Research Letters*, *47*. Retrieved from https://onlinelibrary.wiley.com/doi/10.1029/2020GL087856 doi: 10.1029/2020GL087856

Lin, G., Shearer, P. M., Matoza, R. S., Okubo, P. G., & Amelung, F. (2014, 5). Three-dimensional seismic velocity structure of Mauna Loa and Kilauea volcanoes in Hawaii from local seismic tomography. *Journal of Geophysical Research: Solid Earth*, *119*, 4377-4392. Retrieved from https://onlinelibrary.wiley.com/doi/full/10.1002/2013JB010820https://onlinelibrary.wiley.com/doi/abs/10.1002/2013JB010820https://agupubs.onlinelibrary.wiley.com/doi/10.1002/2013JB010820 doi: 10.1002/2013JB010820

Loewen, M. W. (2021). *Thin section crossed-polarized light photomicrograph of a radial plagioclase phenocryst in a May 25, 2021, Great Sitkin breadcrust bomb.* Alaska Volcano Observatory / U.S. Geological Survey. Retrieved from https://avo.alaska.edu/images/image.php?id=178421

Marchese, F., & Genzano, N. (2022, 10). Global volcano monitoring through the Normalized Hotspot Indices (NHI) system. *Journal of the Geological Society*. Retrieved from https://www.lyellcollection.org/doi/10.1144/jgs2022-014 doi: 10.1144/jgs2022-014

Miller, T. P., McGimsey, R. G., Richter, D. H., Riehle, J. R., Nye, C., Yount, M. E., & Dumoulin, J. A. (1998). Catalog of the historically active volcanoes of Alaska. *Open-File Report*. doi: 10.3133/OFR98582

Norris, A. (1985, 3). A differential scheme for the effective moduli of composites. *Mechanics of Materials*, *4*, 1-16. Retrieved from https://linkinghub.elsevier.com/retrieve/pii/016766368590002X doi: 10.1016/0167-6636(85)90002-X

Patanè, D., Barberi, G., Gori, P. D., Cocina, O., Zuccarello, L., Garcia-Yeguas, A., … Sgroi, T. (2017, 7). The shallow magma chamber of Stromboli Volcano (Italy). *Geophysical Research Letters*, *44*, 6589-6596. Retrieved from https://onlinelibrary.wiley.com/doi/full/10.1002/2017GL073008 doi: 10.1002/2017GL073008

Paulatto, M., Hooft, E. E. E., Chrapkiewicz, K., Heath, B., Toomey, D. R., & Morgan, J. V. (2022, 10). Advances in seismic imaging of magma and crystal mush. *Frontiers in Earth Science*, *10*, 2005. Retrieved from https://www.frontiersin.org/articles/10.3389/feart.2022.970131/full doi: 10.3389/feart.2022.970131

Pesicek, J. D., Thurber, C. H., DeShon, H. R., Prejean, S. G., & Zhang, H. (2008, 10). Three-Dimensional P-Wave Velocity Structure and Precise Earthquake Relocation at Great Sitkin Volcano, Alaska. *Bulletin of the Seismological Society of America*, *98*, 2428-2448. Retrieved from https://pubs.geoscienceworld.org/bssa/article/98/5/2428-2448/350147 doi: 10.1785/0120070213

Power, J. A., Stihler, S., White, R., & Moran, S. (2004, 12). Observations of deep long-period (DLP) seismic events beneath Aleutian arc volcanoes; 1989–2002. *Journal of Volcanology and Geothermal Research*, *138*, 243-266. Retrieved from https://linkinghub.elsevier.com/retrieve/pii/S0377027304002392 doi: 10.1016/j.jvolgeores.2004.07.005

Power, J. A., Villaseñor, A., & Benz, H. M. (1998). Seismic image of the Mount Spurr magmatic system. *Bulletin of Volcanology*, *60*, 27-37. doi: 10.1007/s004450050214

Roman, D. C., & Cashman, K. V. (2018, 9). Top–down precursory volcanic seismicity: Implications for 'stealth' magma ascent and long-term eruption forecasting. *Frontiers in Earth Science*, *6*, 124. doi: 10.3389/FEART.2018.00124/BIBTEX

Roman, D. C., Power, J. A., Moran, S. C., Cashman, K. V., Doukas, M. P., Neal, C. A., & Gerlach, T. M. (2004, 2). Evidence for dike emplacement beneath Iliamna Volcano, Alaska in 1996. *Journal of Volcanology and Geothermal Research*, *130*, 265-284. Retrieved from https://linkinghub.elsevier.com/retrieve/pii/

S0377027303003020 doi: 10.1016/S0377-0273(03)00302-0
Scandone, R., Cashman, K. V., & Malone, S. D. (2007). Magma supply, magma ascent and the style of volcanic eruptions. *Earth and Planetary Science Letters*, *253*(3), 513-529. Retrieved from https://www.sciencedirect.com/science/article/pii/S0012821X06008181 doi: https://doi.org/10.1016/j.epsl.2006.11.016
Shapiro, N. M., & Ritzwoller, M. H. (2002). Monte-Carlo inversion for a global shear-velocity model of the crust and upper mantle. *Geophysical Journal International*, *151*, 88-105. doi: 10.1046/j.1365-246X.2002.01742.x
Sparks, R. S. J., Annen, C., Blundy, J. D., Cashman, K. V., Rust, A. C., & Jackson, M. D. (2019, 2). Formation and dynamics of magma reservoirs. *Philosophical Transactions of the Royal Society A: Mathematical, Physical and Engineering Sciences*, *377*, 20180019. Retrieved from https://royalsocietypublishing.org/doi/10.1098/rsta.2018.0019 doi: 10.1098/rsta.2018.0019
Spera, F. J. (2004, 8). Open-system magma chamber evolution: an energy-constrained geochemical model incorporating the effects of concurrent eruption, recharge, variable assimilation and fractional crystallization (EC-E'RAχC). *Journal of Petrology*, *45*, 2459-2480. Retrieved from https://academic.oup.com/petrology/article-lookup/doi/10.1093/petrology/egh072 doi: 10.1093/petrology/egh072
Takei, Y. (2002, 2). Effect of pore geometry on V_P/V_S: From equilibrium geometry to crack. *Journal of Geophysical Research: Solid Earth*, *107*, ECV 6-1. Retrieved from https://onlinelibrary.wiley.com/doi/full/10.1029/2001JB000522https://onlinelibrary.wiley.com/doi/abs/10.1029/2001JB000522https://agupubs.onlinelibrary.wiley.com/doi/10.1029/2001JB000522 doi: 10.1029/2001JB000522
Tibaldi, A. (2015, 6). Structure of volcano plumbing systems: A review of multi-parametric effects. *Journal of Volcanology and Geothermal Research*, *298*, 85-135. doi: 10.1016/J.JVOLGEORES.2015.03.023
Ueki, K., & Iwamori, H. (2016, 5). Density and seismic velocity of hydrous melts under crustal and upper mantle conditions. *Geochemistry, Geophysics, Geosystems*, *17*, 1799-1814. Retrieved from https://onlinelibrary.wiley.com/doi/full/10.1002/2015GC006242https://onlinelibrary.wiley.com/doi/abs/10.1002/2015GC006242https://agupubs.onlinelibrary.wiley.com/doi/10.1002/2015GC006242 doi: 10.1002/2015GC006242
U.S. Geological Survey. (2022). *ANSS Comprehensive Earthquake Catalog* (Tech. Rep.). Menlo Park, CA: U.S. Geological Survey.
Viens, L., Denolle, M., Miyake, H., Sakai, S., & Nakagawa, S. (2017, 7). Retrieving impulse response function amplitudes from the ambient seismic field. *Geophysical Journal International*, *210*, 210-222. Retrieved from https://academic.oup.com/gji/article-lookup/doi/10.1093/gji/ggx155 doi: 10.1093/gji/ggx155
Ward, K. M., Delph, J. R., Zandt, G., Beck, S. L., & Ducea, M. N. (2017, 12). Magmatic evolution of a cordilleran flare-up and its role in the creation of silicic crust. *Scientific Reports*, *7*, 9047. Retrieved from http://www.nature.com/articles/s41598-017-09015-5 doi: 10.1038/s41598-017-09015-5
Waythomas, C. F., Miller, T. P., & Nye, C. (2003). Preliminary geologic map of Great Sitkin Volcano, Alaska. *USGS Open-File Report*. Retrieved from https://doi.org/10.3133/ofr0336 doi: 10.3133/ofr0336
Yang, X., & Gao, H. (2018). Full-wave seismic tomography in the northeastern United States: New insights into the uplift mechanism of the Adirondack Mountains. *Geophysical Research Letters*, *45*. doi: 10.1029/2018GL078438
Yang, X., & Gao, H. (2020). Segmentation of the Aleutian-Alaska subduction zone revealed by full-wave ambient noise tomography: Implications for the along-strike variation of volcanism. *Journal of Geophysical Research: Solid Earth*, *125*, 1-20. doi: 10.1029/2020JB019677
Yang, X., Zuffoletti, I. D., D'Souza, N. J., & Denolle, M. A. (2022, 1). *SeisGo: A ready-to-go Python toolbox for seismic data analysis* [Computer Software]. Zenodo. Retrieved

from `https://doi.org/10.5281/zenodo.5873724` doi: 10.5281/zenodo.5873724

Zhang, W., Zhang, Z., & Chen, X. (2012). Three-dimensional elastic wave numerical modelling in the presence of surface topography by a collocated-grid finite-difference method on curvilinear grids. *Geophysical Journal International*, *190*, 358-378. doi: 10.1111/j.1365-246X.2012.05472.x

Zhang, Z., & Shen, Y. (2008). Cross-dependence of finite-frequency compressional waveforms to shear seismic wave speeds. *Geophysical Journal International*, *174*, 941-948. doi: 10.1111/j.1365-246X.2008.03840.x

Double reservoirs imaged below Great Sitkin Volcano, Alaska, explain the migration of volcanic seismicity

Xiaotao Yang[1], Diana C. Roman[2], Matt Haney[3], Cody A. Kupres[1]

[1]Department of Earth, Atmospheric, and Planetary Sciences, Purdue University, West Lafayette, IN, USA.
[2]Earth and Planets Laboratory, Carnegie Institution for Science, Washington, DC, USA
[3]Alaska Volcano Observatory, USGS, Anchorage, AK, USA

Key Points:

- The pre- and co-eruptive seismicity below Great Sitkin Volcano, Alaska, shows a strong spatiotemporal migration
- A new 3-D shear-wave velocity model reveals two crustal low-velocity anomalies that correlate with the migrating seismicity
- We propose a six-stage eruption cycle involving two magma reservoirs to explain the long-term and short-term seismicity patterns

Corresponding author: Xiaotao Yang, `xtyang@purdue.edu`

Abstract

Volcanic seismicity provides essential insights into the behavior of an active volcano across multiple time scales. However, to understand how magma moves as an eruption evolves, better knowledge of the geometry and physical properties of the magma plumbing system is required. In this study, using full-wave ambient noise tomography, we image the 3-D crustal shear-wave velocity structure below Great Sitkin Volcano in the central Aleutian Arc. The new velocity model reveals two low-velocity anomalies, which correlate with the migration of volcanic seismicity. With a partial melt of up to about 30%, these low-velocity anomalies are characterized as mushy magma reservoirs. We propose a six-stage eruption cycle to explain the migration of seismicity and the alternating eruption of two reservoirs with different recharging histories. The findings in this study have broad implications for the dynamics of magma plumbing systems and the structural control of eruption behaviors.

Plain Language Summary

Understanding magma accumulation and transport systems below active volcanoes is essential for predicting eruption behavior and assessing the potential hazards. The distribution of earthquakes can partly be used to infer the development of magmatic activity at different times. However, to understand how magma moves at different stages of an eruption cycle, better knowledge of what the magma plumbing system looks like is necessary. In this study, we use an advanced seismic imaging method to construct the 3-D crustal shear-wave velocity structure below Great Sitkin Volcano in the central Aleutian Arc. The new velocity model reveals two crustal magma reservoirs, which correlate with the migration of seismicity. We propose a six-stage eruption cycle to explain the evolution of seismicity in space and time across the island and the alternating eruption of two reservoirs. The findings in this study help to understand better the control of eruption behaviors by the underlying magma plumbing system at active volcanoes.

1 Introduction

Magma plumbing systems of active volcanoes consist of magma storage reservoirs and conduits for transportation of magma to the surface (e.g., Tibaldi, 2015; Chaussard et al., 2013). The geometry and dynamics of magma plumbing systems play an essential role in controlling the eruption behavior. Magma plumbing systems possess a wide range of complexity in terms of the connection and interaction between multiple magma chambers (e.g., Tibaldi, 2015; Huang et al., 2015; Kiser et al., 2021), the lateral offset between reservoirs and the edifice (e.g., Tibaldi, 2015; Lerner et al., 2020), the geochemical evolution of the magma (e.g., Spera, 2004), and the development of eruptive activity in an eruption cycle (e.g., Tibaldi, 2015; Chaussard et al., 2013; Roman & Cashman, 2018; Paulatto et al., 2022). Among these complexities, it is important to understand how magma moves in space and time during an eruption and between eruptions and what controls this process. We address these questions by investigating Great Sitkin Volcano in central Aleutian Arc in Alaska (Figure 1a) (e.g., Miller et al., 1998; Waythomas et al., 2003), which erupted on 26 May 2021 with ongoing effusive lava flows as of the time of writing (Global Volcanism Program, 2022a). Great Sitkin Volcano is an oval-shaped stratovolcano with a collapsed caldera (Waythomas et al., 2003) and an edifice aperture of about 8 by 11 km (Figure 1a) (Miller et al., 1998). The volcanic rocks are dominantly andesites to basaltic andesites (Miller et al., 1998; Waythomas et al., 2003). The ongoing eruption started as an explosive eruption on 26 May 2021 and was preceded by multiple phreatic explosions between June 2018 and February 2019. The 26 May 2021 eruption was followed by a dome emplacement that peaked in growth rate during August through September (Global Volcanism Program, 2022b, 2022a; Marchese & Genzano, 2022).

Seismic activity at volcanoes helps to reveal the evolution of the eruption activity (e.g., Power et al., 2004; Roman et al., 2004; Scandone et al., 2007; Pesicek et al., 2008; Roman & Cashman, 2018). At Great Sitkin, volcanic earthquakes (5/1/2020-9/5/2022) are primarily concentrated along an NW-SE trending zone (Figure 1a). This seismic zone delineates an inverse-V shape in depth, with the shallowest earthquakes below the caldera summit and the 2021 eruption vent (Figure 1a and b). Locations of the pre- and co-eruptive seismicity suggest the migration of magmatic activity (Figure 1b-d). Approximately 24 hours before the 26 May 2021 eruption, seismicity started to increase abruptly (Figure 1c) with a swarm of earthquakes northwest of the edifice (swarm-1 in Figure 1a-b). About two months later, a second earthquake swarm (swarm-2) occurred further to the southeast. Interestingly, about one year after the initial eruption, there was another earthquake swarm (swarm-3) northwest of the edifice, generally at greater depth than swarm-1 earthquakes. In the longer term (Figure 1d), there was an earthquake cluster in early 2002 through 2004 southeast of the edifice (Pesicek et al., 2008). Pesicek et al. (2008) and Power et al. (2004) argue that this cluster of volcano-tectonic earthquakes and the co-occurring long-period events are evidence of a magma intrusion. This elevated seismicity (Figure 1d) suggests that the reservoir to the southeast of the volcano edifice may have begun recharging as early as 2002, reaching its peak in 2020. In contrast, to the northwest of the volcano edifice, there was a slight increase in seismicity in 2018, followed by a relatively seismically quiet period in 2020 until the day before the eruption (Global Volcanism Program, 2022b). However, it is not clear how the migration of seismicity is linked to the geometry and dynamics of the magma plumbing system.

We investigate structural controls of the spatial-temporal migration of seismicity at Great Sitkin Volcano and the associated eruption stages. We construct a 3-D shear-wave velocity model for the upper 6 km of the crust below sea level (BSL) under Great Sitkin, using a full-wave ambient noise tomography method. The new shear-wave velocity model reveals two low-velocity anomalies at 1.5-4.5 km BSL and 3-6 km BSL to the southeast and northwest of the volcano edifice, respectively. These low-velocity anomalies correspond to up to approximately 30% partial melts and are thus characterized as mushy magma

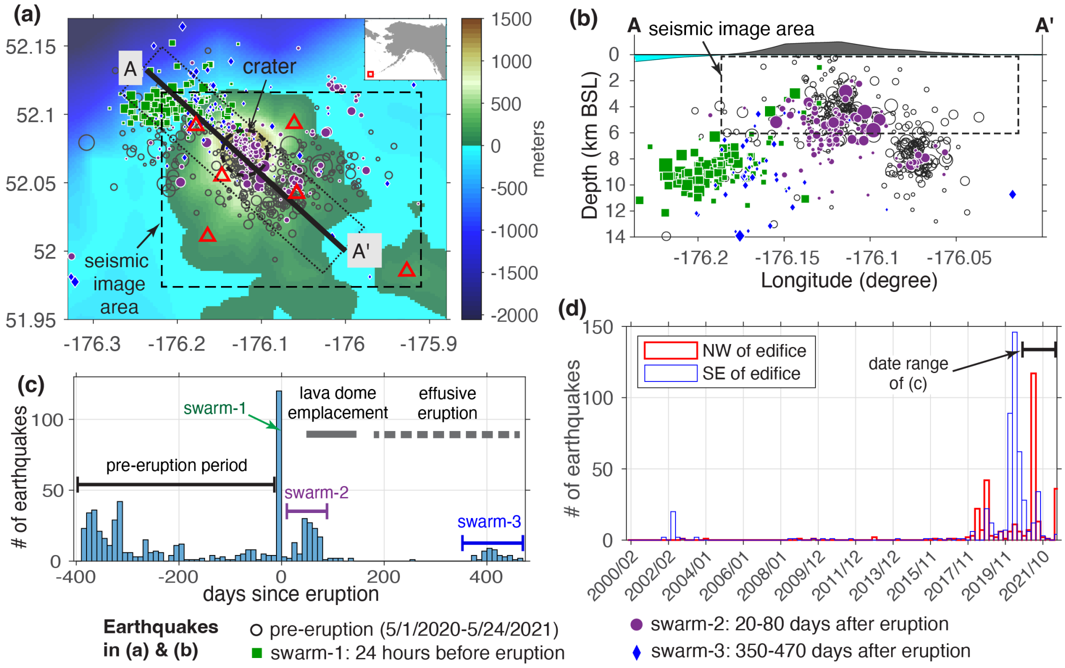

Figure 1. Distribution of earthquakes around Great Sitkin Volcano between different time periods. (a) Earthquake epicenters (magnitude ≥ 0) from the USGS Comprehensive Earthquake Catalog (ComCat) (U.S. Geological Survey, 2022) from May 2020 to September 2022, scaled by magnitude. The main explosive eruption occurred at 5:04 UTC on 26 May 2021. The pre-eruption earthquakes (5/1/2020-5/24/2021) are shown as open circles. Swarm-1 (green squares) refers to earthquakes within approximately 24 hours before the 26 May 2021 eruption. Swarm-2 (purple dots) includes earthquakes 10-100 days after the initial eruption. Swarm-3 (blue diamonds) contains earthquakes 300-470 days after the initial eruption. Triangles are seismic stations from the Alaska Volcano Observatory network (network code: AV) used in this study (Alaska Volcano Observatory/USGS, 1988). The dashed box shows the seismic imaging area. (b) Depth distribution of the earthquakes along profile A-A' highlighting the three earthquake swarms. The dashed box shows the seismic imaging area. BSL: below sea level. (c) Histogram with 10-day bins showing the variation of seismicity within 2 km from profile A-A', shown as the dotted box in (a). The three earthquake swarms are labeled along with the key development phases of the eruption. (d) Histograms with 90-day bins showing the longer-term variations of seismicity between 1/1/2000 and 9/5/2022 to the northwest (thick red bars) and southeast (thin blue bars) of the volcano edifice. The earthquakes below the crater atop the edifice, with the lateral extent defined by the dashed circle in (a), are excluded in (d).

reservoirs. We propose a six-stage eruption cycle to explain the spatiotemporal migration of the volcanic seismicity at Great Sitkin.

2 Data and Methods

2.1 Empirical Green's functions

Empirical Green's functions between two seismic stations can be retrieved from the cross-correlations of ambient noise waveforms. We use the *SeisGo* Python toolbox to download the continuous seismic waveforms and compute the cross-correlations (Yang et al., 2022). The Alaska Volcano Observatory operates six broadband seismic stations on Great Sitkin Island and nearby Igitkin Island (network code: AV; triangles in Figure 1a) (Alaska Volcano Observatory/USGS, 1988). We download the vertical continuous waveforms from these stations between 7/1/2019 and 8/1/2020 from the IRIS Data Management Center. We downsample the waveforms at the rate of 20 Hz, followed by the removal of the instrument responses.

We slice the continuous waveforms into 4-hour segments with a step of 2 hours and normalize the amplitude spectrum of each segment using the moving average method, as described by Bensen et al. (2007). We attempt to further eliminate transient signals by discarding segments with peak amplitudes greater than 10 times the standard deviation of all segments within each downloaded 3-day block, following Jiang and Denolle (2020). We then compute the cross-correlations in the frequency domain following Viens et al. (2017). We calculate the stacks of the cross-correlations across the entire duration and within each 30-day window to provide uncertainties of the phase delay measurements in Section 2.2. The empirical Green's functions are computed as the negative time derivative of the cross-correlations.

2.2 Full-wave ambient noise tomography

We apply the full-wave ambient noise tomography method, which involves full-wavefield simulation, to invert for the velocity perturbations using finite-frequency kernels (e.g., Gao & Shen, 2012, 2014; Yang & Gao, 2018, 2020). The tomography method accounts for the cross-dependence of Rayleigh waves to both P and S wave velocities (Z. Zhang & Shen, 2008). We first simulate the wave propagation in the 3-D spherical Earth using a nonstaggered-grid, finite-difference method (W. Zhang et al., 2012), with a grid spacing of 0.001 and 0.0013 degrees in the latitudinal and longitudinal directions, respectively. The vertical grid spacing increases with depth from 0.037 km at the surface to 0.022 km at the depth of 28 km. We use the global velocity model by Shapiro and Ritzwoller (2002) as the reference model. We then measure the Rayleigh wave phase delays between the synthetics and the observed empirical Green's functions through cross-correlations in eight overlapping period ranges, including 0.6-1s, 0.8-1.25s, 1-1.5s, 1.25-1.8s, 1.5-2s, 1.8-2.5s, 2-3s, and 2.5-3.5s. Before measuring the phase delays, we discard empirical Green's functions with signal-to-noise ratios below 3. The phase delay measurements with correlation coefficients ≥ 0.6 are used in the kernel calculation and inversion. The reference velocity model is progressively updated for four iterations until major velocity features converge to achieve the final model.

3 Results: Shear-Wave Velocity Model

The shear-wave velocity model reveals two low-velocity features at different depths aligning in the northwest-southeast direction (L1 and L2 in Figure 2). At a depth of 2 km (Figure 2a-b), we observe a prominent, localized low-velocity feature (1-1.2 km/s) beneath station GSMY (anomaly L1). This anomaly extends down to about 3-4 km BSL, where the velocity is about 1.5-2.1 km/s (Figure S1a). At greater depths (Figures 2c and S1a), the velocity generally decreases toward the northwest with a low-velocity anomaly of 2.2-2.6 km/s in the broad region below station GSSP (anomaly L2). The vertical velocity cross-section A-A' (NW-SE across the island) shows the separation of these two low-velocity anomalies (with up to -10% perturbations) in both lateral and vertical directions (Figure 2d). Both of these two low-velocity anomalies, particularly L1, appear to be dipping to the northwest (Figure 2d), though the top of the L1 anomaly is not well-constrained. The NW-SE alignment of these two low-velocity anomalies is consistent with the location of the NW-SE trending seismic zone (Figures 1a and 2a-c). The cross-sections along profiles B-B' and C-C' show that the L1 low-velocity anomaly is localized in the SW-NE direction and is bounded by higher velocities extending down to at least 6 km BSL, below which our resolution is dramatically decreased, as described below.

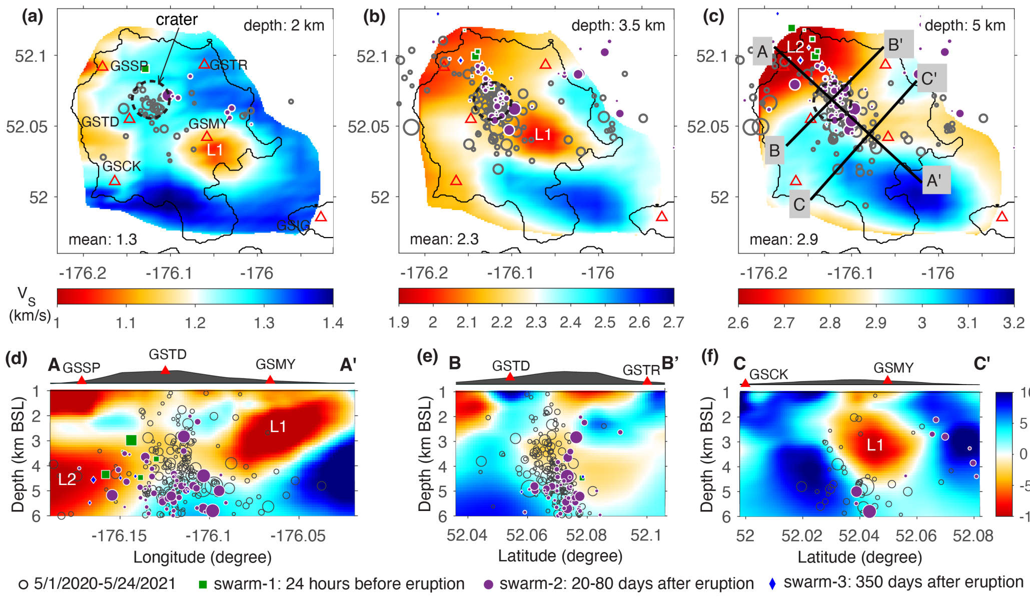

Figure 2. Shear-wave velocity model of Great Sitkin. (a)-(c) Velocity depth slices at 2 km, 3.5 km, and 5 km BSL, respectively. The average velocity at each depth is given in the lower-left corner of each panel. The triangles are AV seismic stations. Earthquakes are projected about ± 1 km around the slice depth, scaled by magnitudes. Gray circles are earthquakes between 5/1/2020 and 5/24/2021. Earthquake swarm-1 (green squares), swarm-2 (purple dots), and swarm-3 (blue diamonds) are shown for reference, color-coded the same as Figure 1a. The dashed circle marks the extent of the crater atop the volcano edifice. L1 and L2 label the two key low-velocity features. (d)-(f) Vertical cross-sections of the shear-wave velocity model at 1-6 km BSL, showing the velocity perturbations relative to the average velocity at each depth. Since the absolute velocities span across a wide range from 1 km/s to about 3.5 km/s (Figure S1), we use perturbations to highlight the velocity anomalies. Earthquakes are projected within about 2 km away from each profile, color-coded as in (a)-(c). See panel (c) for the profile locations.

The checkerboard resolution tests (Figure S3) and model recovery tests (Figure S4) suggest that our best resolution is for the depth range of 2-5 km BSL, degrading dramatically at greater depths. We can resolve the geometry of velocity anomalies with a horizontal scale of >3.5 km and a vertical scale of > 2 km. In addition, L1 can be resolved much better than L2 (Figure S4). In later sections, when analyzing the absolute velocities or perturbation amplitudes, we focus more on the L1 anomaly. See Text S1 in the supplement for a detailed resolution analysis.

4 Discussion

4.1 Correlation with seismicity

The key features in the new velocity model show a strong correlation with the earthquake activity below Great Sitkin Island. The earthquakes from 5/1/2020 to 9/5/2022 are concentrated between these two low-velocity anomalies mainly at the depth of > 2 km BSL (L1 and L2 in Figure 2d). The centers of both L1 and L2 anomalies are relatively aseismic (Figure 2d and f). Below the depth of 4 km, the earthquakes are concentrated along relatively large velocity gradients (Figure 2d). This concentration pattern has been observed at other active volcanoes, such as Mount St. Helens Volcano in the Cascadia volcanic arc (e.g., Barker & Malone, 1991; Kiser et al., 2016), Mount Spurr Volcano in southwestern Alaska (Power et al., 1998), the Hawaiian volcanoes (Lin et al., 2014), Redoubt Volcano in Alaska (Benz et al., 1996), Stromboli Volcano in Italy (Patanè et al., 2017), Mount Rainier Volcano in Cascadia (Flinders & Shen, 2017), and the Gakkel Ridge volcanic complex (Korger & Schlindwein, 2014). The occurrence of earthquakes along velocity gradients below volcanic areas is commonly attributed to the stress concentration at structural boundaries resulting from magma movement or dike intrusion (e.g., Korger & Schlindwein, 2014; Barker & Malone, 1991; Roman et al., 2004; Kiser et al., 2016).

The earthquake swarms before and after the 26 May 2021 initial eruption provides insights into the eruption dynamics. Occurring right before the eruption, swarm-1 earthquakes may delineate the magma pathway (with a relatively fast ascent rate)for the initial eruption, suggesting it was sourced from the L2 reservoir. Swarm-2 earthquakes occurred during the dome emplacement period (late July 2021 through November 2021; Figure 1c), primarily along the velocity gradient at the bottom of the L1 anomaly and below the edifice. This spatiotemporal coincidence indicates that the L1 anomaly may be linked to the dome emplacement. The seismicity at a shallower depth (i.e., < 2 km BSL) likely delineates shallow magma conduits, which seem to be shared by swarm-1 and swarm-2 (Figure 1b). However, the detailed geometry and velocity of the shallow conduit are not resolvable in our model. The distinct difference in the inferred intrusion timelines between the southeast and the northwest of the edifice is coincident with the spatial separation of the two low-velocity anomalies (L1 and L2) below these two regions.

4.2 Double magma reservoirs

There are multiple mechanisms that can reduce shear-wave velocities at active volcanoes, including high-temperature anomalies (e.g., Kern et al., 2001), volatiles (water and gas) (e.g., Ito, 1990; Chu et al., 2010; Christensen & Stanley, 2003), and partial melts (e.g., Avellaneda, 1987; Berryman, 1998; Norris, 1985; Takei, 2002; Paulatto et al., 2022). Considering the surface heat flow and the distribution of geothermal features at Great Stikin Island, the contributions from temperature anomalies to the L1 and L2 low-velocity anomalies should be minor (see Text S2 in the supplement). Water and gas are likely to play an important role in reducing the shear-wave velocities, though the exact contribution is not well constrained with the current data on water content and gas emissions (e.g., Fischer et al., 2021). On the other hand, partial melts are commonly used to explain seismic low velocities below active volcanoes (e.g., Lees, 2007; Lin et al., 2014; Power et al., 1998; Jaxybulatov et al., 2014; Kiser et al., 2016; Ward et al., 2017; Delph et al., 2017; Paulatto et al., 2022). With the ongoing eruption of the Great Sitkin Volcano, it is reasonable to assume partial melts as the dominant factor responsible for the velocity reduction of the L1 and L2 anomalies.

The melt fraction estimates for L1 and L2 low-velocity anomalies suggest that they are mushy magma reservoirs with up to approximately 30% partial melts. At Great Sitkin, the volcanic deposits are dominantly andesite and basaltic andesite (Miller et al., 1998; Loewen, 2021). We compute the melt fractions following the workflow and computer codes by Paulatto et al. (2022) using the Self-Consistent Scheme (Figure S5a) (e.g, Berryman, 1998; Paulatto et al., 2022) and the Differential Effective Medium (Figure S5b) (e.g., Norris, 1985; Avellaneda, 1987; Paulatto et al., 2022) methods. We use velocities for crystal and molten andesite based on the experimental data by Christensen and Stanley (2003), Ueki and Iwamori (2016), and Takei (2002) (see Text S3 in the supplement for key parameters). The estimated melt fractions are about 0.23 ± 0.1 and about 0.11 ± 0.05 for the L1 and L2 anomalies, respectively. Because of the limited resolution in recovering the synthetic L2 anomaly (Text S1), the uncertainty of the melt fraction for L2 is relatively large. It is worth noting that these estimates are the upper limits without considering volatiles. Measurements of the volatile contents from this volcano, as done for other volcanoes along the Aleutian

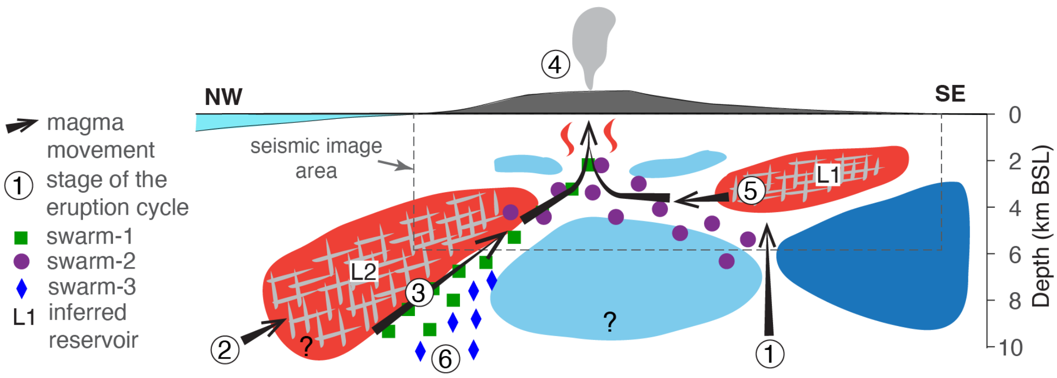

Figure 3. Schematic model showing the six-stage evolution of the 2021-present eruption of the Great Sitkin Volcano. Stage-1: recharge of the L1 reservoir southeast of the edifice. Stage-2: recharge of the L2 reservoir northwest of the edifice. Stage-3: magma ascent and intense fracturing along the lower boundary of the L2 reservoir. Stage-4: explosive eruption with magma primarily from the L2 reservoir. Stage-5: initial dome emplacement with magma primarily from the L1 reservoir. Stage-6: prolonged effusive eruption with magma sourced from the L2 reservoir. The structures within the dashed box are interpreted based on cross-section A-A' (Figure 2d). The question marks denote extrapolated structures that are not constrained by the velocity model.

Arc (Fischer et al., 2019, 2021), would help refine the melt estimates. Nevertheless, the partial melts within the L1 and L2 anomalies are evidence of mushy magma reservoirs.

4.3 A six-stage eruption cycle

The spatial and temporal migration of seismicity before and after the 26 May 2021 explosive eruption (Figure 1) indicates a complicated eruption cycle, spanning at least 20 years. This eruption cycle likely consists of multiple stages, with added complexity from the interaction of the two inferred magma reservoirs. Previous studies have proposed several models to explain multi-stage magma unrest and eruption based on seismicity (e.g., Roman & Cashman, 2018), surface deformation (e.g., Chaussard et al., 2013), and petrological and geochemical characteristics (e.g., Spera, 2004; Sparks et al., 2019). However, these models mostly focus on the vertical migration of magma activity as the eruption cycle evolves. They cannot explain the bi-modal behaviors of the spatially separated (both laterally and vertically) magma reservoirs below Great Sitkin Volcano.

We propose a six-stage eruption cycle for the 26 May 2021 eruption of the Great Sitkin Volcano, involving the imaged deep (L2) and shallow (L1) reservoirs (Figure 3). This model explains the observations from both long- and short-term seismicity (Figure 1) and seismic velocity structures (Figure 2). It is a refined development of the seismicity and geochemical evolution models by Spera (2004) and Roman and Cashman (2018). The key development of our model is the consideration of the interaction and alternation between magma reservoirs. We describe the six stages of the eruption cycle in the following paragraphs.

Stage-1: Recharge of the shallow reservoir (L1). At this stage, the shallow (L1) reservoir southeast of the edifice associated with L1 low-velocity anomaly starts to recharge, as inferred from the cluster of earthquakes and long-period events (Power et al., 2004; Pesicek et al., 2008). The magma is likely fed through a nearly vertical pathway down to at least 12 km, which is the bottom of the earthquake cluster (Pesicek et al., 2008). Although the resolution is low, this pathway might align with the northwestern boundary of the relatively high velocities below the L1 reservoir (Figure 2d). The recharge of the

L1 reservoir reaches its peak intensity in 2020, corresponding to the elevated seismicity in late 2020 that decreased in early 2021 (Figure 1d). It is worth noting that Pesicek et al. (2008) also identified another cluster of earthquakes in March 2002 about 20 km to the west of the volcano edifice at the depth of >10 km BSL (beyond our study area). Although they argue that these earthquakes are not volcanic events, we cannot completely rule out the possibility of magma intrusion at this location based on current constraints. Therefore, there is a slight chance that there was another magma intrusion in early 2002 further to the west of the edifice (west of the L2 reservoir).

Stage-2: Recharge of the deep reservoir (L2). About 15-16 years after the initial recharge of the L1 reservoir, the L2 reservoir west-northwest of the volcano edifice starts to recharge in late 2017. The recharging process is accompanied by a moderate increase in earthquake activity lasting through 2020 (Figure 1d). In contrast to the recharge of the L1 reservoir, the lapse is much shorter for the L2 reservoir between the initial recharge and the eruption. Stages 1 and 2 correspond to the staging phase by Roman and Cashman (2018) and Spera (2004) but happen at two reservoirs. The current data is insufficient to evaluate the potential connection of the deep sources feeding these two reservoirs.

Stage-3: Rapid magma ascent from the L2 reservoir. As magma recharge continues, the pressure within the L2 reservoir slowly builds up to the critical value, causing intensive fracturing and accelerated ascent of the magma along the lower boundary of the L2 reservoir. This boundary, with fractures, serves as the pathway for magma to quickly move toward the volcano summit. This magma pathway is delineated by NW-dipping swarm-1 seismic zone and a relatively large seismic velocity gradient (Figure 2d).

Stage-4: Explosive eruption sourced from the L2 reservoir. The intense fracturing and magma ascent processes lead to an explosive eruption within 24 hours. Based on the location of swarm-1 earthquakes, the eruption at this stage is driven mostly by the magma activity of the L2 reservoir. The drop in seismicity in this region in late 2020, likely associated with the L1 reservoir, suggests a possible depressurization, such as through inflation (e.g., Chaussard et al., 2013). However, more data on surface deformation is needed to test this hypothesis.

Stage-5: Dome formation sourced from the L1 reservoir. About 2 months following the initial eruption, an intensive dome emplacement phase begins, accompanied by a swarm of earthquakes generally below the L1 and L2 reservoirs (swarm-2) (Figure 1c). As implied by the seismicity, the dome emplacement might be driven by the magma from both reservoirs, explaining the rapid dome growth from July to October 2021 (Global Volcanism Program, 2022a). However, most of the swarm-2 earthquakes are located below the L1 reservoir, suggesting that the L1 reservoir dominates the magma activity at this stage. This stage is an important development compared to previously proposed eruption cycles (e.g., Roman & Cashman, 2018; Spera, 2004; Chaussard et al., 2013), as it implies dynamic interaction between the reservoirs. Specifically, the eruption and fast magma transport of the L2 reservoir may have created fractures that helped to unseal the L1 reservoir. The magma moves toward the conduits even when the pressure is below the critical point with relatively low seismicity. This explains why the dome emplacement is more effusive than explosive. Eruption modeling and petrological analyses (e.g. Larsen et al., 2013; Biggs et al., 2016), which are outside the scope of this study, would help examine this phenomenon of successive tapping of two reservoirs during the eruption. The conduits or fractures produced by the explosive eruption of the L2 reservoir would make it easy for the magma in the L1 reservoir to flow out. Nevertheless, the lateral transport of magma is commonly seen or proposed at other volcanoes (e.g., Tibaldi, 2015; Lerner et al., 2020; Kiser et al., 2021). A more detailed seismic imaging with improved station coverage is required to narrow down the explanations.

Stage-6: Resurgence of the deeper L2 reservoir. As the eruption becomes more effusive and dome emplacement slows down, magmatic activity switches back to the deeper

L2 reservoir. This is supported by a cluster of small earthquakes below the L2 reservoir (swarm-3), overall deeper than swarm-1 earthquakes. The magma activity in the L1 reservoir decays during this stage. Stages 3-6 involve a model of two active reservoirs that alternate as sources of the eruption.

4.4 Future studies

With two magma reservoirs, migrating volcanic seismicity, and a collapsed caldera, Great Sitkin Volcano provides an ideal natural laboratory to study the dynamics of magma plumbing systems and volcanic hazards. Due to the limited data coverage, there are several remaining questions to be addressed by future studies about the eruption dynamics at Great Sitkin with multi-disciplinary observations. A better constraint on the lateral and depth scales of the L2 reservoir requires a larger aperture seismic array. Denser station coverage is needed to image the distribution of shallow magma conduits below the summit and to understand their control of magma transport and the eruption explosivity. Data on surface deformation (e.g., InSAR mapping) would help to examine the surface inflation and deflation corresponding to different eruption stages. The record of surface temperature over the past several years and its spatial distribution would help refine the temperature anomaly at different stages as well as the estimate of melt fractions. Measurements of volatile emissions from the volcano would also improve melt fraction estimates. In addition, a high-resolution gravity survey is required to delineate the heterogeneity of density below the island.

5 Conclusions

The geometry and dynamics of magma plumbing systems play an essential role in controlling the eruption behavior of active volcanoes. Furthermore, the distribution of earthquakes provides essential insights into the magma transport below the volcano. At Great Sitkin Volcano in the central Aleutian Arc, Alaska, which erupted on 26 May 2021 and continues with ongoing effusive lava flows, the seismicity patterns during the past two decades show a strong migration across the volcanic island from northwest to southeast of the edifice. Multiple swarms of earthquakes have occurred at different locations as the eruption cycle evolved. We construct a 3-D crustal shear-wave velocity model of Great Sitkin Island for the upper 6 km of the crust BSL, which reveals two low-velocity anomalies corresponding to mushy magma reservoirs with up to approximately 30% partial melts. We propose a six-stage eruption cycle to explain the migration of seismicity and the alternating eruption of the two reservoirs with different recharging histories. The findings in this study have broad implications for the dynamics of magma plumbing systems and the structural control of eruption behavior.

Open Research

The seismic waveforms from the Alaska Volcano Observatory network (Alaska Volcano Observatory/USGS, 1988) were downloaded from IRIS Data Management Center (`https://ds.iris.edu/ds/nodes/dmc/`) and processed using *SeisGo* (`https://doi.org/10.5281/zenodo.5873724`), built upon *ObsPy* (Beyreuther et al., 2010) and *NoisePy* (Jiang & Denolle, 2020).

Acknowledgments
This research has been funded by the startup funding of Purdue University for Xiaotao Yang.
Author Contributions: X. Yang contributed to conceptualization, supervision, funding acquisition, data curation, methodology, formal analysis, interpretation, and writing of the original draft. D. Roman, M. Haney, and C. Kupres all contributed to the interpretation and reviewing and editing of the manuscript.

References

Alaska Volcano Observatory/USGS. (1988). *Alaska Volcano Observatory* (Tech. Rep.). Anchorage, AK: International Federation of Digital Seismograph Networks. doi: 10.7914/SN/AV

Avellaneda, M. (1987, 9). Iterated homogenization, differential effective medium theory and applications. *Communications on Pure and Applied Mathematics*, *40*, 527-554. Retrieved from `https://onlinelibrary.wiley.com/doi/full/10.1002/cpa.3160400502` doi: 10.1002/CPA.3160400502

Barker, S. E., & Malone, S. D. (1991, 7). Magmatic system geometry at Mount St. Helens modeled from the stress field associated with posteruptive earthquakes. *Journal of Geophysical Research*, *96*, 11883. Retrieved from `http://doi.wiley.com/10.1029/91JB00430` doi: 10.1029/91JB00430

Bensen, G. D., Ritzwoller, M. H., Barmin, M. P., Levshin, A. L., Lin, F., Moschetti, M. P., ... Yang, Y. (2007). Processing seismic ambient noise data to obtain reliable broadband surface wave dispersion measurements. *Geophysical Journal International*, *169*, 1239-1260. doi: 10.1111/j.1365-246X.2007.03374.x

Benz, H. M., Chouet, B. A., Dawson, P. B., Lahr, J. C., Page, R. A., & Hole, J. A. (1996, 4). Three-dimensional *P* and *S* wave velocity structure of Redoubt Volcano, Alaska. *Journal of Geophysical Research: Solid Earth*, *101*, 8111-8128. Retrieved from `http://doi.wiley.com/10.1029/95JB03046` doi: 10.1029/95JB03046

Berryman, J. G. (1998, 6). Long-wavelength propagation in composite elastic media ii. ellipsoidal inclusions. *The Journal of the Acoustical Society of America*, *68*, 1820. Retrieved from `https://asa.scitation.org/doi/abs/10.1121/1.385172` doi: 10.1121/1.385172

Beyreuther, M., Barsch, R., Krischer, L., Megies, T., Behr, Y., & Wassermann, J. (2010, 05). ObsPy: A Python Toolbox for Seismology. *Seismological Research Letters*, *81*(3), 530-533. Retrieved from `https://doi.org/10.1785/gssrl.81.3.530` doi: 10.1785/gssrl.81.3.530

Biggs, J., Robertson, E., & Cashman, K. (2016, 4). The lateral extent of volcanic interactions during unrest and eruption. *Nature Geoscience*, *9*, 308-311. Retrieved from `http://www.nature.com/articles/ngeo2658` doi: 10.1038/ngeo2658

Chaussard, E., Amelung, F., & Aoki, Y. (2013, 8). Characterization of open and closed volcanic systems in Indonesia and Mexico using InSAR time series. *Journal of Geophysical Research: Solid Earth*, *118*, 3957-3969. Retrieved from `https://onlinelibrary.wiley.com/doi/full/10.1002/jgrb.50288https://onlinelibrary.wiley.com/doi/abs/10.1002/jgrb.50288https://agupubs.onlinelibrary.wiley.com/doi/10.1002/jgrb.50288` doi: 10.1002/JGRB.50288

Christensen, N. I., & Stanley, D. (2003). Seismic velocities and densities of rocks. *International Geophysics*, *81*, 1587-1594. doi: 10.1016/S0074-6142(03)80278-4

Chu, R., Helmberger, D. V., Sun, D., Jackson, J. M., & Zhu, L. (2010, 1). Mushy magma beneath yellowstone. *Geophysical Research Letters*, *37*. doi: 10.1029/2009GL041656

Delph, J. R., Ward, K. M., Zandt, G., Ducea, M. N., & Beck, S. L. (2017). Imaging a magma plumbing system from mash zone to magma reservoir. *Earth and Planetary Science Letters*, *457*, 313-324. Retrieved from `www.elsevier.com/locate/epsl` doi: 10.1016/j.epsl.2016.10.008

Fischer, T. P., Arellano, S., Carn, S., Aiuppa, A., Galle, B., Allard, P., ... Chiodini, G. (2019, 12). The emissions of CO_2 and other volatiles from the world's subaerial volcanoes. *Scientific Reports 2019 9:1*, *9*, 1-11. Retrieved from `https://www.nature.com/articles/s41598-019-54682-1` doi: 10.1038/s41598-019-54682-1

Fischer, T. P., Lopez, T. M., Aiuppa, A., Rizzo, A. L., Ilanko, T., Kelley, K. A., & Cottrell, E. (2021, 12). Gas emissions from the western Aleutians volcanic arc. *Frontiers in Earth Science*, *9*, 1205. Retrieved from `https://www.frontiersin.org/articles/10.3389/feart.2021.786021/full` doi: 10.3389/feart.2021.786021

Flinders, A. F., & Shen, Y. (2017, 12). Seismic evidence for a possible deep crustal hot zone beneath southwest Washington. *Scientific Reports*, *7*, 7400. Retrieved from

http://www.nature.com/articles/s41598-017-07123-w doi: 10.1038/s41598-017-07123-w
Gao, H., & Shen, Y. (2012). Validation of shear-wave velocity models of the Pacific Northwest. *Bulletin of the Seismological Society of America*, *102*, 2611-2621. doi: 10.1785/0120110336
Gao, H., & Shen, Y. (2014). Upper mantle structure of the Cascades from full-wave ambient noise tomography: Evidence for 3d mantle upwelling in the back-arc. *Earth and Planetary Science Letters*, *390*, 222-233. doi: 10.1016/j.epsl.2014.01.012
Global Volcanism Program. (2022a, May). *Report on Great Sitkin (United States)* (Vol. 47) (No. 5). Smithsonian Institution.
Global Volcanism Program. (2022b, September). *Report on Great Sitkin (United States)* (Vol. 43) (No. 9). Smithsonian Institution. Retrieved from https://doi.org/10.5479/si.GVP.BGVN201809-311120
Huang, H. H., Lin, F. C., Schmandt, B., Farrell, J., Smith, R. B., & Tsai, V. C. (2015). The Yellowstone magmatic system from the mantle plume to the upper crust. *Science*, *348*, 773-776. doi: 10.1126/science.aaa5648
Ito, K. (1990, 1). Effects of H_2O on elastic wave velocities in ultrabasic rocks at 900°C under 1 GPa. *Physics of the Earth and Planetary Interiors*, *61*, 260-268. Retrieved from https://linkinghub.elsevier.com/retrieve/pii/003192019090110J doi: 10.1016/0031-9201(90)90110-J
Jaxybulatov, K., Shapiro, N. M., Koulakov, I., Mordret, A., Landes, M., & Sens-Schonfelder, C. (2014, 10). A large magmatic sill complex beneath the Toba caldera. *Science*, *346*, 617-619. Retrieved from https://www.sciencemag.org/lookup/doi/10.1126/science.1258582 doi: 10.1126/science.1258582
Jiang, C., & Denolle, M. A. (2020). Noisepy: A new high-performance python tool for ambient-noise seismology. *Seismological Research Letters*. Retrieved from https://pubs.geoscienceworld.org/ssa/srl/article/583390/NoisePy-A-New-HighPerformance-Python-Tool-for doi: 10.1785/0220190364
Kern, H., Popp, T., Gorbatsevich, F., Zharikov, A., Lobanov, K., & Smirnov, Y. (2001, 8). Pressure and temperature dependence of v_p and v_s in rocks from the superdeep well and from surface analogues at kola and the nature of velocity anisotropy. *Tectonophysics*, *338*, 113-134. Retrieved from https://linkinghub.elsevier.com/retrieve/pii/S0040195101001287 doi: 10.1016/S0040-1951(01)00128-7
Kiser, E., Levander, A., Schmandt, B., & Hansen, S. (2021, 3). Seismic evidence of bottom-up crustal control on volcanism and magma storage near Mount St. Helens. *Geophysical Research Letters*, *48*, e2020GL090612. Retrieved from https://onlinelibrary.wiley.com/doi/full/10.1029/2020GL090612https://onlinelibrary.wiley.com/doi/abs/10.1029/2020GL090612https://agupubs.onlinelibrary.wiley.com/doi/10.1029/2020GL090612 doi: 10.1029/2020GL090612
Kiser, E., Palomeras, I., Levander, A., Zelt, C., Harder, S., Schmandt, B., ... Ulberg, C. (2016). Magma reservoirs from the upper crust to the moho inferred from high-resolution v_p and v_s models beneath Mount St. Helens, Washington State, USA. *GEOLOGY*, *44*. Retrieved from www.geosociety.org/pubs/ft2016.htm, doi: 10.1130/G37591.1
Korger, E., & Schlindwein, V. (2014, 1). Seismicity and structure of the 85°E volcanic complex at the ultraslow spreading Gakkel Ridge from local earthquake tomography. *Geophysical Journal International*, *196*, 539-551. Retrieved from http://academic.oup.com/gji/article/196/1/539/592594/Seismicity-and-structure-of-the-85E-volcanic doi: 10.1093/gji/ggt390
Larsen, J. F., Śliwiński, M. G., Nye, C., Cameron, C., & Schaefer, J. R. (2013, 8). The 2008 eruption of Okmok Volcano, Alaska: Petrological and geochemical constraints on the subsurface magma plumbing system. *Journal of Volcanology and Geothermal Research*, *264*, 85-106. Retrieved from https://linkinghub.elsevier.com/retrieve/pii/S0377027313002217 doi: 10.1016/j.jvolgeores.2013.07.003

Lees, J. M. (2007, 11). Seismic tomography of magmatic systems. *Journal of Volcanology and Geothermal Research*, *167*, 37-56. Retrieved from https://linkinghub.elsevier.com/retrieve/pii/S0377027307001965 doi: 10.1016/j.jvolgeores.2007.06.008

Lerner, A. H., O'Hara, D., Karlstrom, L., Ebmeier, S. K., Anderson, K. R., & Hurwitz, S. (2020, 7). The prevalence and significance of offset magma reservoirs at arc volcanoes. *Geophysical Research Letters*, *47*. Retrieved from https://onlinelibrary.wiley.com/doi/10.1029/2020GL087856 doi: 10.1029/2020GL087856

Lin, G., Shearer, P. M., Matoza, R. S., Okubo, P. G., & Amelung, F. (2014, 5). Three-dimensional seismic velocity structure of Mauna Loa and Kilauea volcanoes in Hawaii from local seismic tomography. *Journal of Geophysical Research: Solid Earth*, *119*, 4377-4392. Retrieved from https://onlinelibrary.wiley.com/doi/full/10.1002/2013JB010820https://onlinelibrary.wiley.com/doi/abs/10.1002/2013JB010820https://agupubs.onlinelibrary.wiley.com/doi/10.1002/2013JB010820 doi: 10.1002/2013JB010820

Loewen, M. W. (2021). *Thin section crossed-polarized light photomicrograph of a radial plagioclase phenocryst in a May 25, 2021, Great Sitkin breadcrust bomb.* Alaska Volcano Observatory / U.S. Geological Survey. Retrieved from https://avo.alaska.edu/images/image.php?id=178421

Marchese, F., & Genzano, N. (2022, 10). Global volcano monitoring through the Normalized Hotspot Indices (NHI) system. *Journal of the Geological Society*. Retrieved from https://www.lyellcollection.org/doi/10.1144/jgs2022-014 doi: 10.1144/jgs2022-014

Miller, T. P., McGimsey, R. G., Richter, D. H., Riehle, J. R., Nye, C., Yount, M. E., & Dumoulin, J. A. (1998). Catalog of the historically active volcanoes of Alaska. *Open-File Report*. doi: 10.3133/OFR98582

Norris, A. (1985, 3). A differential scheme for the effective moduli of composites. *Mechanics of Materials*, *4*, 1-16. Retrieved from https://linkinghub.elsevier.com/retrieve/pii/016766368590002X doi: 10.1016/0167-6636(85)90002-X

Patanè, D., Barberi, G., Gori, P. D., Cocina, O., Zuccarello, L., Garcia-Yeguas, A., ... Sgroi, T. (2017, 7). The shallow magma chamber of Stromboli Volcano (Italy). *Geophysical Research Letters*, *44*, 6589-6596. Retrieved from https://onlinelibrary.wiley.com/doi/full/10.1002/2017GL073008 doi: 10.1002/2017GL073008

Paulatto, M., Hooft, E. E. E., Chrapkiewicz, K., Heath, B., Toomey, D. R., & Morgan, J. V. (2022, 10). Advances in seismic imaging of magma and crystal mush. *Frontiers in Earth Science*, *10*, 2005. Retrieved from https://www.frontiersin.org/articles/10.3389/feart.2022.970131/full doi: 10.3389/feart.2022.970131

Pesicek, J. D., Thurber, C. H., DeShon, H. R., Prejean, S. G., & Zhang, H. (2008, 10). Three-Dimensional P-Wave Velocity Structure and Precise Earthquake Relocation at Great Sitkin Volcano, Alaska. *Bulletin of the Seismological Society of America*, *98*, 2428-2448. Retrieved from https://pubs.geoscienceworld.org/bssa/article/98/5/2428-2448/350147 doi: 10.1785/0120070213

Power, J. A., Stihler, S., White, R., & Moran, S. (2004, 12). Observations of deep long-period (DLP) seismic events beneath Aleutian arc volcanoes; 1989–2002. *Journal of Volcanology and Geothermal Research*, *138*, 243-266. Retrieved from https://linkinghub.elsevier.com/retrieve/pii/S0377027304002392 doi: 10.1016/j.jvolgeores.2004.07.005

Power, J. A., Villaseñor, A., & Benz, H. M. (1998). Seismic image of the Mount Spurr magmatic system. *Bulletin of Volcanology*, *60*, 27-37. doi: 10.1007/s004450050214

Roman, D. C., & Cashman, K. V. (2018, 9). Top–down precursory volcanic seismicity: Implications for 'stealth' magma ascent and long-term eruption forecasting. *Frontiers in Earth Science*, *6*, 124. doi: 10.3389/FEART.2018.00124/BIBTEX

Roman, D. C., Power, J. A., Moran, S. C., Cashman, K. V., Doukas, M. P., Neal, C. A., & Gerlach, T. M. (2004, 2). Evidence for dike emplacement beneath Iliamna Volcano, Alaska in 1996. *Journal of Volcanology and Geothermal Research*, *130*, 265-284. Retrieved from https://linkinghub.elsevier.com/retrieve/pii/

S0377027303003020 doi: 10.1016/S0377-0273(03)00302-0
Scandone, R., Cashman, K. V., & Malone, S. D. (2007). Magma supply, magma ascent and the style of volcanic eruptions. *Earth and Planetary Science Letters*, *253*(3), 513-529. Retrieved from https://www.sciencedirect.com/science/article/pii/S0012821X06008181 doi: https://doi.org/10.1016/j.epsl.2006.11.016
Shapiro, N. M., & Ritzwoller, M. H. (2002). Monte-Carlo inversion for a global shear-velocity model of the crust and upper mantle. *Geophysical Journal International*, *151*, 88-105. doi: 10.1046/j.1365-246X.2002.01742.x
Sparks, R. S. J., Annen, C., Blundy, J. D., Cashman, K. V., Rust, A. C., & Jackson, M. D. (2019, 2). Formation and dynamics of magma reservoirs. *Philosophical Transactions of the Royal Society A: Mathematical, Physical and Engineering Sciences*, *377*, 20180019. Retrieved from https://royalsocietypublishing.org/doi/10.1098/rsta.2018.0019 doi: 10.1098/rsta.2018.0019
Spera, F. J. (2004, 8). Open-system magma chamber evolution: an energy-constrained geochemical model incorporating the effects of concurrent eruption, recharge, variable assimilation and fractional crystallization (EC-E'RAχC). *Journal of Petrology*, *45*, 2459-2480. Retrieved from https://academic.oup.com/petrology/article-lookup/doi/10.1093/petrology/egh072 doi: 10.1093/petrology/egh072
Takei, Y. (2002, 2). Effect of pore geometry on V_P/V_S: From equilibrium geometry to crack. *Journal of Geophysical Research: Solid Earth*, *107*, ECV 6-1. Retrieved from https://onlinelibrary.wiley.com/doi/full/10.1029/2001JB000522https://onlinelibrary.wiley.com/doi/abs/10.1029/2001JB000522https://agupubs.onlinelibrary.wiley.com/doi/10.1029/2001JB000522 doi: 10.1029/2001JB000522
Tibaldi, A. (2015, 6). Structure of volcano plumbing systems: A review of multi-parametric effects. *Journal of Volcanology and Geothermal Research*, *298*, 85-135. doi: 10.1016/J.JVOLGEORES.2015.03.023
Ueki, K., & Iwamori, H. (2016, 5). Density and seismic velocity of hydrous melts under crustal and upper mantle conditions. *Geochemistry, Geophysics, Geosystems*, *17*, 1799-1814. Retrieved from https://onlinelibrary.wiley.com/doi/full/10.1002/2015GC006242https://onlinelibrary.wiley.com/doi/abs/10.1002/2015GC006242https://agupubs.onlinelibrary.wiley.com/doi/10.1002/2015GC006242 doi: 10.1002/2015GC006242
U.S. Geological Survey. (2022). *ANSS Comprehensive Earthquake Catalog* (Tech. Rep.). Menlo Park, CA: U.S. Geological Survey.
Viens, L., Denolle, M., Miyake, H., Sakai, S., & Nakagawa, S. (2017, 7). Retrieving impulse response function amplitudes from the ambient seismic field. *Geophysical Journal International*, *210*, 210-222. Retrieved from https://academic.oup.com/gji/article-lookup/doi/10.1093/gji/ggx155 doi: 10.1093/gji/ggx155
Ward, K. M., Delph, J. R., Zandt, G., Beck, S. L., & Ducea, M. N. (2017, 12). Magmatic evolution of a cordilleran flare-up and its role in the creation of silicic crust. *Scientific Reports*, *7*, 9047. Retrieved from http://www.nature.com/articles/s41598-017-09015-5 doi: 10.1038/s41598-017-09015-5
Waythomas, C. F., Miller, T. P., & Nye, C. (2003). Preliminary geologic map of Great Sitkin Volcano, Alaska. *USGS Open-File Report*. Retrieved from https://doi.org/10.3133/ofr0336 doi: 10.3133/ofr0336
Yang, X., & Gao, H. (2018). Full-wave seismic tomography in the northeastern United States: New insights into the uplift mechanism of the Adirondack Mountains. *Geophysical Research Letters*, *45*. doi: 10.1029/2018GL078438
Yang, X., & Gao, H. (2020). Segmentation of the Aleutian-Alaska subduction zone revealed by full-wave ambient noise tomography: Implications for the along-strike variation of volcanism. *Journal of Geophysical Research: Solid Earth*, *125*, 1-20. doi: 10.1029/2020JB019677
Yang, X., Zuffoletti, I. D., D'Souza, N. J., & Denolle, M. A. (2022, 1). *SeisGo: A ready-to-go Python toolbox for seismic data analysis* [Computer Software]. Zenodo. Retrieved

from https://doi.org/10.5281/zenodo.5873724 doi: 10.5281/zenodo.5873724

Zhang, W., Zhang, Z., & Chen, X. (2012). Three-dimensional elastic wave numerical modelling in the presence of surface topography by a collocated-grid finite-difference method on curvilinear grids. *Geophysical Journal International*, *190*, 358-378. doi: 10.1111/j.1365-246X.2012.05472.x

Zhang, Z., & Shen, Y. (2008). Cross-dependence of finite-frequency compressional waveforms to shear seismic wave speeds. *Geophysical Journal International*, *174*, 941-948. doi: 10.1111/j.1365-246X.2008.03840.x

Supporting Information for

Double reservoirs imaged below Great Sitkin Volcano, Alaska, explain the migration of volcanic seismicity

Xiaotao Yang[1], Diana C. Roman[2], Matt Haney[3], Cody A. Kupres[1]

[1]Department of Earth, Atmospheric, and Planetary Sciences, Purdue University, West Lafayette, IN, USA.

[2]Earth and Planets Laboratory, Carnegie Institution for Science, Washington, DC, USA

[3]Alaska Volcano Observatory, USGS, Anchorage, AK, USA

Contents of this file

Introduction

This supplementary file contains additional text and figures to support the main text, including resolution test results, absolute velocity cross-sections, and comparison with the reference model.

Text S1. Resolution analysis

Overall, the final shear-wave velocity model from the full-wave ambient noise tomography is greatly improved compared to the reference model, showing more details below the volcanic island (Figure S2). The maximum resolvable depth is determined by the array's aperture (nominally about 10 km). However, limited by the sparse station coverage, we could only resolve seismic features at a horizontal scale of about 3.5 km and above within the top 5-6 km (Figures S3 and S4a-S4b). Figure S4c-S4d in the supplement shows that the overall geometry of L1 can be recovered with about 20-30% amplitude recovery above the depth of 5 km. The velocity anomalies below the depth of about 5 km, including the low-velocity L2, are mainly carried from the reference model (Figure S2a-S2c in the supplement) and are poorly resolved by the current data coverage. In terms of amplitudes of the anomalies, we could resolve about 20% of the input velocity perturbation in the top 3-4 km, decreasing to about 10-15% at greater depths. This suggests that while the key relative velocity perturbation patterns could be resolved at a scale of 3.5 km and above, the amplitudes of the velocity anomaly might be greatly underestimated. The underestimation of the perturbation amplitudes is partly due to the damping and smoothing operations as needed to stabilize the inversion process. Informed by the resolution test results, we limit our discussion to those velocity features with a horizontal scale of >3.5 km and a vertical scale of > 2 km.

Text S2. Minor contributions to shear-wave velocity reduction from no-melt mechanisms

The contribution of a temperature anomaly and active fractures to the reduction of shear-wave velocity is negligible. The surface heat flow at the Great Sitkin island, with a sample location northwest of the edifice, is about 97 mW/m^2, similar to the measurements at most of the active Alaska volcanoes (Batir et al., 2016; Batir, 2017). With only one data point, we don't have control over the lateral variation of the surface heat flow and subsurface temperature anomalies across the island. Some geothermal features, including fumaroles, mud pots, and hot springs, are only observed at the southern flank of the edifice, away from the imaged low-velocity anomalies. The reduction of shear-wave velocities is about 0.5% per 100°C relative to the average shear velocity of 3.65 km/s for a variety of dry rock types (Kern et al., 2001). To fully account for the 10% velocity reduction for L1 and L2 anomalies, with a surface temperature of 20°C, the estimated temperature anomaly would be about 2000°C, which is unrealistically high and is much higher than the melting temperature for minerals in the dry andesite. Even with an extremely high geothermal gradient of 100°C/km as in some active volcanoes (Lowell et al., 2014), the temperature at 4 km depth would be 420°C. This is about 300°C higher than the temperature computed with a geothermal gradient of 25°C/km, contributing to about 1.5% shear-wave velocity reduction. On the other hand, the lack of earthquakes within the imaged low-velocity anomalies rules out the existence of active fractures as a major contribution.

Text S3. Parameters in estimating the melt fractions for L1 and L2 low-velocity anomalies

At the Great Sitkin island, the volcanic deposits are dominantly andesite and basaltic andesite (Miller et al., 1998; Loewen, 2021). Following the procedures and computer codes by Paulatto et al. (2022), we compute the melt fractions for the L1 and L2 low-velocity anomalies (Figure S5). The shear-wave velocity ranges for L1 (1.5-2.1 km/s) and L2 (2.2-2.6 km/s) are estimated between 2-4 km depth and 4-5.5 km depth, respectively, from Figure S1a. We use the Python Jupyter notebook by Paulatto et al. (2022) to compute the melt fraction curves modified for andesite at a depth of 4 km with a density of 2.627 g/cm^3 (about the pressure of 100 MPa). We use 5.445 km/s and 3.005 km/s as the P- and S-wave velocities, respectively, for andesite crystals, as extrapolated based on a second-order polynomial fit of the values in Christensen and Stanley (2003). For dry molten andesite rocks, we use a density of 2.55 g/cm^3 and a P-wave velocity of 2.594 km/s, scaled down from the value by Ueki and Iwamori (2016) at 1 GPa. S-wave velocity is zero for the pure melt. We use two methods, the Self-Consistent Scheme method (Figure S5a) (e.g, Berryman, 1998; Paulatto et al., 2022) and the Differential Effective Medium method (Figure S5b) (e.g., Norris, 1985; Avellaneda, 1987; Paulatto et al., 2022), to estimate the uncertainties in melt fractions. We compute the melt fractions with a range of spheroidal melt inclusion aspect ratios for dry andesite. We adopt the aspect ratio of 0.1-0.15 (Takei, 2002) to calculate the most probable range of the melt fractions associated with the L1 and L2 anomalies. The melt fractions are about 0.23±0.1 and about 0.11±0.05 for the L1 and L2 anomalies, respectively.

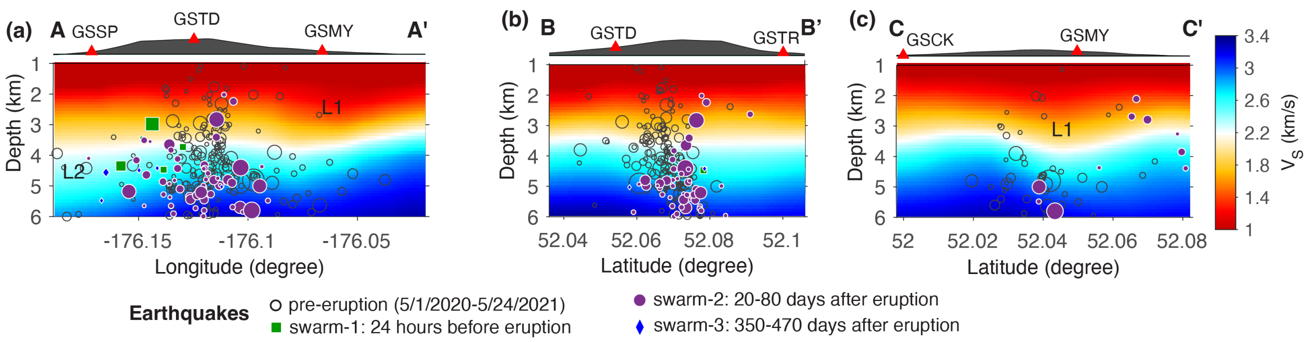

Figure S1. Vertical cross-sections of the shear-wave velocity model between 1-6 km depths showing the absolute velocities. Gray circles are magnitude ≥ 0 earthquakes between 5/1/2020 and 5/24/2021, projected within about 2 km of each profile. Earthquake swarms associated with the 5/26/2021 eruption are also projected with the same parameter. See Figure 2c in the main text for profile locations.

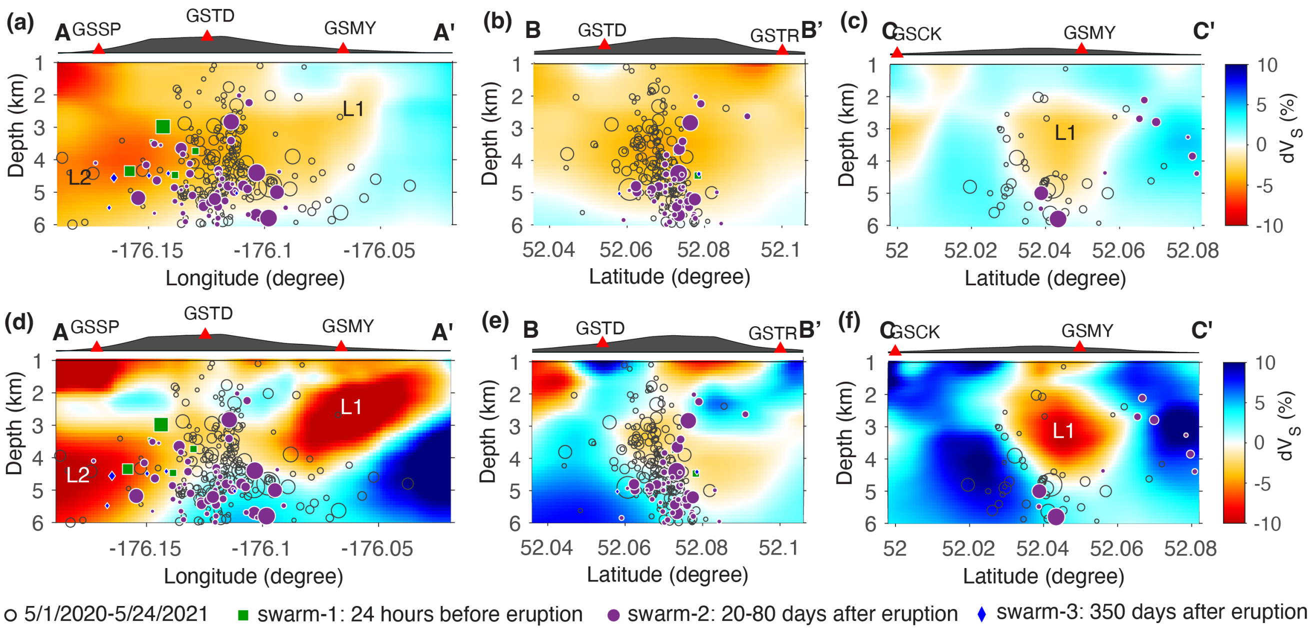

Figure S2. Comparison of cross-sections between the reference velocity model (top) and the final model by this study. The projected earthquakes are the same as in Figure S1. See Figure 2c in the main text for profile locations.

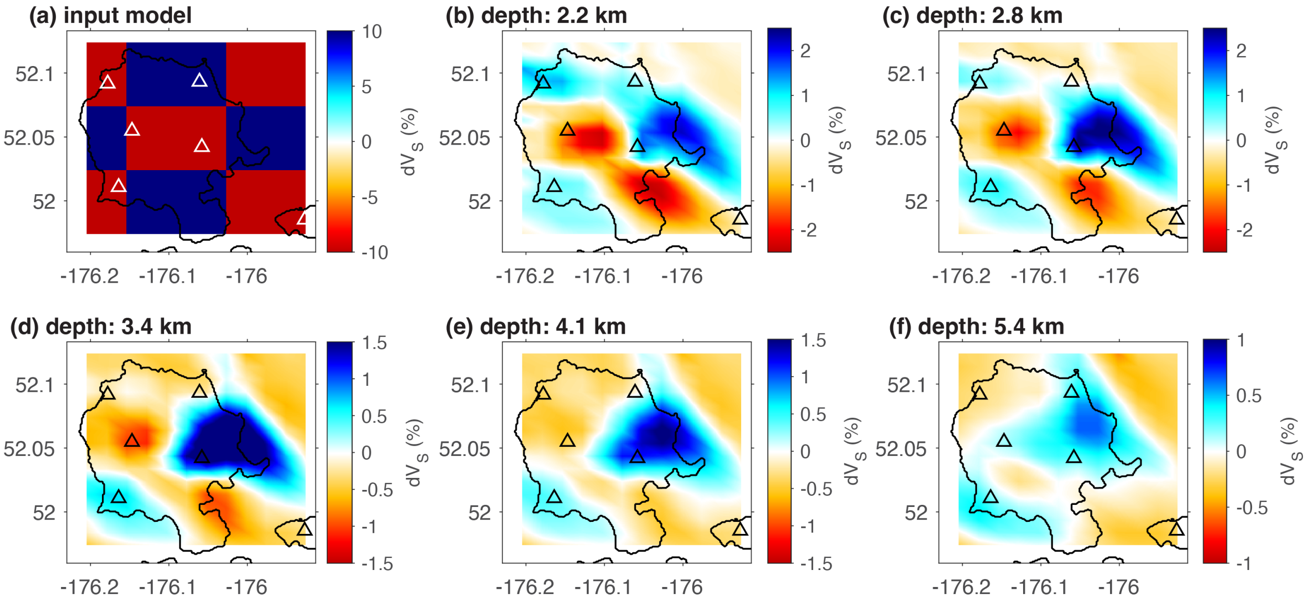

Figure S3. Checkerboard resolution test results. (a) Input checkerboard model at all depths with a perturbation of $\pm 10\%$. (b)-(f) Recovered checkerboard results with the input model in (a) at depths of (b) 2.2 km, (c) 2.8 km, (d) 3.4 km, (e) 4.1 km, and (f) 5.4 km. The triangles are the seismic stations. Different color ranges are chosen in (b)-(f) to highlight the recovered checkerboard patterns.

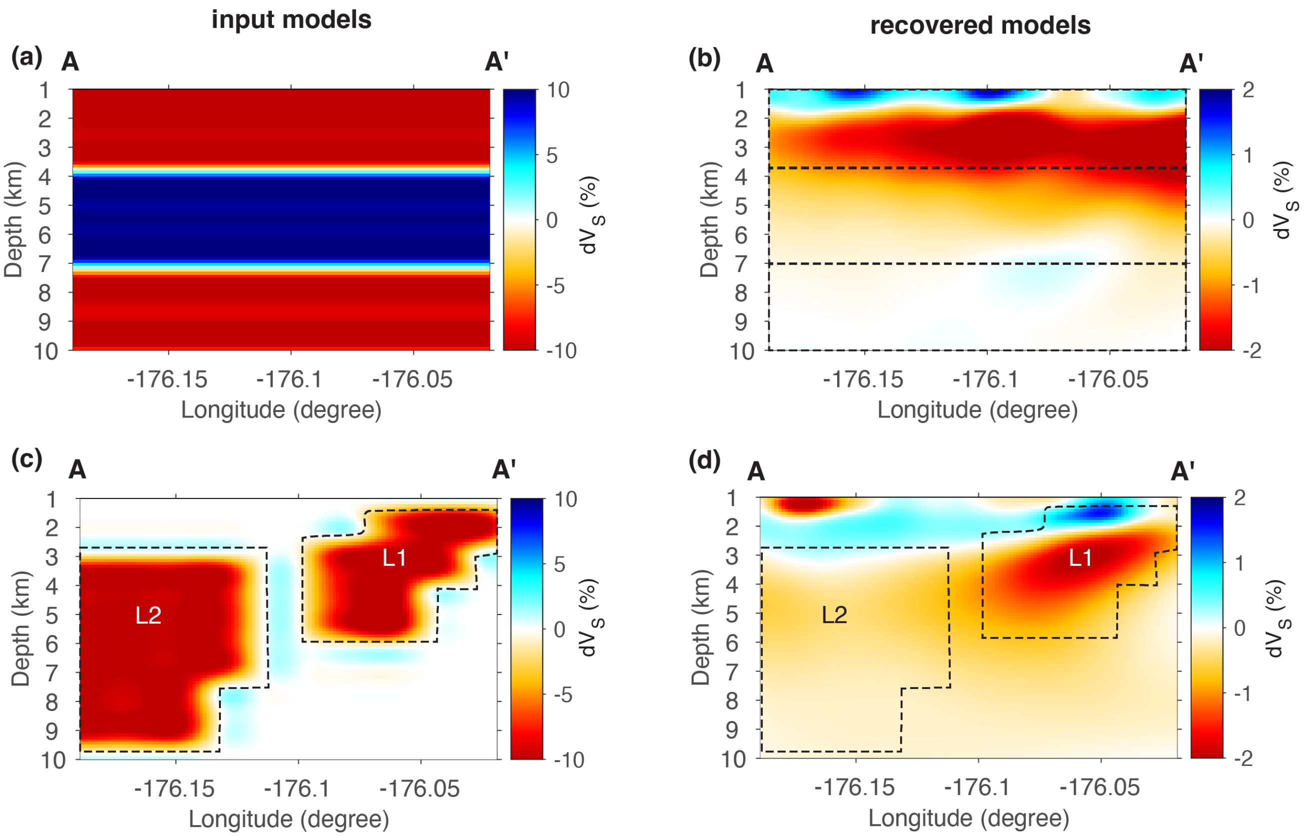

Figure S4. Recovery test results with input models on the left and recovered models on the right. (a-b) A layered model with a thickness of about 3.5 km. (c-d) Results for input low-velocity anomalies simulating the two low-velocity anomalies (L1 and L2) observed in Figure 2d in the main text.

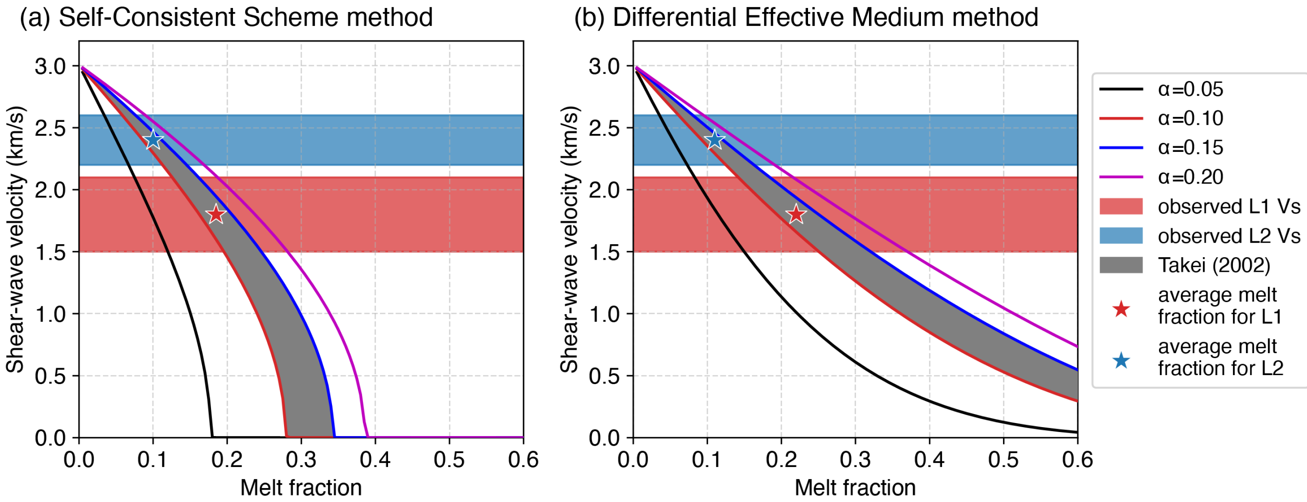

Figure S5. Estimates of the andesite melt fractions for L1 (red star) and L2 (blue star) low-velocity anomalies using two different methods. (a) The relationship between melt fraction and shear-wave velocities estimated using the Self-Consistent Scheme method (e.g, Berryman, 1998; Paulatto et al., 2022). (b) Same as (a) but using the Differential Effective Medium method (e.g., Norris, 1985; Avellaneda, 1987; Paulatto et al., 2022). The curves in (a-b) are color-coded by the aspect ratios (α) of the spheroidal melt inclusions. The gray shaded area marks the aspect ratios suggested by Takei (2002). The red and blue shaded areas mark the ranges of shear-wave velocities for L1 and L2 anomalies, respectively.

References

Avellaneda, M. (1987, 9). Iterated homogenization, differential effective medium theory and applications. *Communications on Pure and Applied Mathematics*, *40*, 527-554. Retrieved from https://onlinelibrary.wiley.com/doi/full/10.1002/cpa.3160400502 doi: 10.1002/CPA.3160400502

Batir, J. F. (2017). *Thermal studies of alaska and british columbia: Examining thermotectonic provinces, climate change, and crustal evolution* (PhD Dissertation, Southern Methodist University). Retrieved from https://www.proquest.com/dissertations-theses/thermal-studies-alaska-british-columbia-examining/docview/1917413401/se-2

Batir, J. F., Blackwell, D. D., & Richards, M. C. (2016). Heat flow and temperature-depth curves throughout alaska: Finding regions for future geothermal exploration. *Journal of Geophysics and Engineering*, *13*, 366-377. doi: 10.1088/1742-2132/13/3/366

Berryman, J. G. (1998, 6). Long-wavelength propagation in composite elastic media ii. ellipsoidal inclusions. *The Journal of the Acoustical Society of America*, *68*, 1820. Retrieved from https://asa.scitation.org/doi/abs/10.1121/1.385172 doi: 10.1121/1.385172

Christensen, N. I., & Stanley, D. (2003). Seismic velocities and densities of rocks. *International Geophysics*, *81*, 1587-1594. doi: 10.1016/S0074-6142(03)80278-4

Kern, H., Popp, T., Gorbatsevich, F., Zharikov, A., Lobanov, K., & Smirnov, Y. (2001, 8). Pressure and temperature dependence of v_p and v_s in rocks from the superdeep well and from surface analogues at kola and the nature of velocity anisotropy. *Tectonophysics*, *338*, 113-134. Retrieved from https://linkinghub.elsevier.com/retrieve/pii/S0040195101001287 doi: 10.1016/S0040-1951(01)00128-7

Loewen, M. W. (2021). *Thin section crossed-polarized light photomicrograph of a radial plagioclase phenocryst in a May 25, 2021, Great Sitkin breadcrust bomb.* Alaska Volcano Observatory / U.S. Geological Survey. Retrieved from https://avo.alaska.edu/images/image.php?id=178421

Lowell, R., Kolandaivelu, K., & Rona, P. (2014). Hydrothermal activity. In *Reference module in earth systems and environmental sciences.* Elsevier. Retrieved from https://www.sciencedirect.com/science/article/pii/B9780124095489091326 doi: https://doi.org/10.1016/B978-0-12-409548-9.09132-6

Miller, T. P., McGimsey, R. G., Richter, D. H., Riehle, J. R., Nye, C., Yount, M. E., & Dumoulin, J. A. (1998). Catalog of the historically active volcanoes of Alaska. *Open-File Report*. doi: 10.3133/OFR98582

Norris, A. (1985, 3). A differential scheme for the effective moduli of composites. *Mechanics of Materials*, *4*, 1-16. Retrieved from https://linkinghub.elsevier.com/retrieve/pii/016766368590002X doi: 10.1016/0167-6636(85)90002-X

Paulatto, M., Hooft, E. E. E., Chrapkiewicz, K., Heath, B., Toomey, D. R., & Morgan, J. V. (2022, 10). Advances in seismic imaging of magma and crystal mush. *Frontiers in Earth Science*, *10*, 2005. Retrieved from https://www.frontiersin.org/articles/10.3389/feart.2022.970131/full doi: 10.3389/feart.2022.970131

Takei, Y. (2002, 2). Effect of pore geometry on V_P/V_S: From equilibrium geometry to crack. *Journal of Geophysical Research: Solid Earth*, *107*, ECV 6-1. Retrieved from https://onlinelibrary.wiley.com/doi/full/10.1029/2001JB000522https://onlinelibrary.wiley.com/doi/abs/10.1029/2001JB000522https://agupubs

.onlinelibrary.wiley.com/doi/10.1029/2001JB000522 doi: 10.1029/2001JB000522

Ueki, K., & Iwamori, H. (2016, 5). Density and seismic velocity of hydrous melts under crustal and upper mantle conditions. *Geochemistry, Geophysics, Geosystems*, *17*, 1799-1814. Retrieved from https://onlinelibrary.wiley.com/doi/full/10.1002/2015GC006242https://onlinelibrary.wiley.com/doi/abs/10.1002/2015GC006242https://agupubs.onlinelibrary.wiley.com/doi/10.1002/2015GC006242 doi: 10.1002/2015GC006242